

Radio properties of high-redshift galaxies at $z \geq 1$

M. Khabibullina,^{1*} A. Mikhailov,¹ Yu. Sotnikova,^{1,2} T. Mufakharov,^{1,2} M. Mingaliev,^{1,2,3} A. Kudryashova,¹ N. Bursov,¹ V. Stolyarov,^{1,4} R. Uдовитский¹

¹Special Astrophysical Observatory, Russian Academy of Sciences, Nizhny Arkhyz, 369167, Russia

²Kazan (Volga Region) Federal University, Kazan 420008, Russia

³Institute of Applied Astronomy, Russian Academy of Sciences, St. Petersburg 191187, Russia

⁴Astrophysics Group, Cavendish Laboratory, University of Cambridge, Cambridge, CB3 0HE, UK

ABSTRACT

Study of high-redshift radio galaxies (HzRGs) can shed light on the active galactic nuclei (AGNs) evolution in massive elliptical galaxies. The vast majority of observed high-redshift AGNs are quasars, and there are very few radio galaxies at redshifts $z > 3$. We present the radio properties of 173 sources optically identified with radio galaxies at $z \geq 1$ with flux densities $S_{1.4} \geq 20$ mJy. Literature data were collected for compilation of broadband radio spectra, estimation of radio variability, radio luminosity, and radio loudness. Almost 60% of the galaxies have steep or ultra-steep radio spectra; 22% have flat, inverted, upturn, and complex spectral shapes, and 18% have peaked spectra (PS). The majority of the PS sources in the sample (20/31) are megahertz-peaked spectrum sources candidates, i.e. possibly very young and compact radio galaxies. The median values of the variability indices at 11 and 5 GHz are $V_{S_{11}} = 0.14$ and $V_{S_5} = 0.13$, which generally indicates a weak or moderate character of the long-term variability of the studied galaxies. The typical radio luminosity and radio loudness are $L_5 = 10^{43} - 10^{44}$ erg s $^{-1}$ and $\log R = 3 - 4$ respectively. We have found less prominent features of the bright compact radio cores for our sample compared to high-redshift quasars at $z \geq 3$. The variety of the obtained radio properties shows the different conditions for the formation of radio emission sources in galaxies.

Key words: galaxies: active – galaxies: high-redshift – quasars: general – radio continuum: galaxies

1 INTRODUCTION

Distant galaxies with redshifts $z > 1$ and radio luminosities $L_{500\text{MHz}}$ exceeding 10^{34} erg s $^{-1}$ are classified as powerful radio galaxies (Miley & De Breuck 2008) with large z – HzRG. These are very rare objects with a density of approximately 10^{-8} Mpc $^{-3}$ for the redshift range ($2 \leq z < 5$). Their spectral energy distribution includes radiation from the dust and stellar components as well as radiation of the active nucleus. Studies of the first two components show that HzRGs are among the most massive galaxies in the Universe (Seymour et al. 2007; Bryant et al. 2009; De Breuck et al. 2010) and are thought to be the progenitors of the massive ellipticals we observe today (Matthews et al. 1964).

These facts allow the radio galaxies to be used as tools for the study of the visible and dark matter distributions, dynamics of the Universe, and the history of its structure formation. The parameters determined from observed data include the age of the galaxy (Verkhodanov et al. 1999, 2001, 2000a), which is limited by the age of the Universe and cannot exceed the latter, since galaxies need certain time to form after the birth of the Universe. A striking feature of radio galaxies is that we observe them virtually from their formation

epoch, i.e., their radio sources are so powerful that modern radio surveys have catalogued almost all objects of this type (Verkhodanov & Parijskij 2008). Such objects can serve as good probes for the study of the formation of galaxy clusters. Therefore, constructing samples of radio galaxies from various redshift ranges is one of the most important tasks in observational cosmology.

A correlation that has frequently been used to search for HzRGs, but is still under debate, is the spectral index to redshift relation (“ $\alpha - z$ ”), where radio sources with steeper spectra appear to be preferentially associated with higher redshift sources (Tielens et al. 1979; De Breuck et al. 2000; Miley & De Breuck 2008). One of the mechanisms that has been suggested to explain this relation is that this is a result of the increased inverse Compton (IC) losses at higher redshifts due to the higher energy density of the cosmic microwave background (CMB) (e.g., Ghisellini et al. 2014 or Klamer et al. 2006). Recently, by modelling a large number of sources over a wide range of redshifts using the Broadband Radio Astronomy Tools¹ (Harwood et al. 2013, 2015), Morabito & Harwood (2018) found that IC losses could indeed be the primary driver behind the “ $\alpha - z$ ” relation. There are two other scenarios that could result in this relation,

* E-mail: rita@sao.ru

¹ <http://www.askanastronomer.co.uk/brats/>

one connected with observational biases and the other related to the environment of the galaxy. A denser medium at high redshift would keep the radio lobes more confined and would result in higher surface brightness for older radio emission coming from the low-energy electron populations. If at higher redshifts radio galaxies preferentially lie in denser environments, these effects could lead to the observed relation. Another effect from the increased ambient density is related to the acceleration of electrons in or near the hotspot.

Although as yet there is no general common consensus on the nature of the “ α – z ” correlation, the very fact that this empirical dependence exists is important for research. An example of an object selected in this way is the radio galaxy that is the redshift record-holder with $z = 5.19$ and its spectral index² $\alpha = -1.63$ at 0.365–1.4 GHz range (van Breugel et al. 1999). Another example is the object RC 0311+0507 investigated in the “Big Trio” Program (Kopylov et al. 2006). Its redshift $z = 4.514$, it has the record radio luminosity for radio galaxies with $z > 4$, and its spectral index $\alpha = -1.31$ at 0.365–4.85 GHz range.

The peaked spectrum shape in the extragalactic radio sources that are characterized by steep optically thin spectra and a spectral turnover in the GHz domain is considered an indicator of young radio sources due to their small size. These AGNs are subdivided into compact steep-spectrum (CSS), gigahertz peaked-spectrum (GPS), and high-frequency peaked (HFP) sources. The CSS sources have typical turnover frequencies in the observer’s frame of reference smaller than 500 MHz and linear sizes (LS) of 1–20 kpc (O’Dea 1998). The GPS and HFP sources have LS < 1 kpc with $0.5 \leq \nu_{\text{peak,obs}} \leq 5$ GHz and $\nu_{\text{peak,obs}} > 5$ GHz respectively (Dallacasa et al. 2000). Additionally the anticorrelation between the rest frame turnover frequency and the projected linear size for the GPS and CSS sources supports assumptions about their evolutionary connection (Fanti et al. 1990; O’Dea & Baum 1997). Compact PS sources with an observed turnover frequency below 1 GHz have also been referred to as megahertz peaked-spectrum (MPS) sources (Coppejans et al. 2015, 2016a,b; Falcke et al. 2004). It is believed that they are a combination of relatively nearby CSS/GPS sources and more distant high-frequency peakers with the peak frequency shifted to low frequencies due to the cosmological redshift.

Investigation of the nature of PS sources can help to understand the features of AGN evolution. Some studies have shown that the peaked spectrum of high-redshift quasars is formed mainly due to the dominant contribution of radio emission from the bright compact core (Snellen et al. 1998; Sotnikova et al. 2021). Many known extremely distant AGNs, at $z > 5$, are blazars and have a peaked radio spectrum (for example, Romani et al. (2004); Frey et al. (2010); Liu et al. (2016); Coppejans et al. (2017); Spingola et al. (2020); Mufakharov et al. (2021)). Such a spectral shape prevails at higher redshifts, where bright jet-beamed blazars are easily discovered. However, the steepening of the spectral index with increasing redshift has not yet been revealed (Ker et al. 2012; Singh et al. 2014; Smolčić et al. 2014). One of the reasons is the poor statistics for distant radio sources.

² Determined in assumption of the power law relation between the flux density S_ν at a frequency ν and the spectral index α : $S_\nu \sim \nu^\alpha$.

At the same time, it should not be ruled out that AGNs can evolve in different ways and such a correlation is natural.

In order to study the nature of HzRGs and their evolution, it is important to obtain a large sample of such objects. Nowadays databases and identification techniques allow automating the search and identification of distant radio galaxies. The catalog of HzRGs can be used not only to perform just purely cosmological studies but also to carry out statistical analysis of identification lists and corresponding populations at different wavelengths (Verkhodanov & Trushkin 2000; Verkhodanov et al. 2003; Balayan & Verkhodanov 2004; Trushkin 2003), to search for and analyze the properties of radio galaxies (Verkhodanov et al. 1999; Verkhodanov 1994; Verkhodanov & Verkhodanova 1999; Parijskij et al. 1999; Verkhodanov et al. 2008; Solovyov & Verkhodanov 2014a,b), and to simulate radio astronomical surveys at different telescopes (Gorokhov & Verkhodanov 1994; Khabibullina et al. 2008; Majorova 2008).

Such a catalog of radio galaxies with redshifts $z \geq 0.3$ has been previously constructed by the authors Khabibullina & Verkhodanov (2009a,b,c). The catalog contains 2442 sources with redshifts, photometric magnitudes, and flux densities in the radio band; the sizes of the radio sources, the coordinates, and the radio spectral indices were calculated from the results of cross-identification with the radio catalogs from the CATS³ database (Verkhodanov et al. 1997, 2005).

In this paper we collect a sample of 173 bright radio galaxies, with spectral flux density more than 20 mJy at 1.4 GHz (hereafter we indicate the frequency in lowercase index), with spectroscopic redshifts $z \geq 1$, based on the data from the NED⁴, SDSS⁵ (Lyke et al. 2020), CATS, and VizieR Information System⁶ (Ochsenbein et al. 2000). We present their radio properties, radio spectra classification, radio variability parameters at a long time scale up to 30 years, radio loudness and radio luminosity estimates. We propose new MPS, GPS, and HFP candidates and estimate their fraction among bright radio galaxies at high redshifts. Several infrared properties of AGNs have been analyzed.

2 THE SAMPLE

To build the primary list, we used the NED database, where we selected objects with the following parameters: redshifts $z \geq 1$, flux densities at 1.4 GHz $S_{1.4} \geq 20$ mJy, classified as a galaxy. The initial list contained 9000 objects. This sample was polluted by objects with differing properties. So the next stage consisted in cleaning the initial sample from wrong sources. To this end, we selected the following objects to be removed from the initial sample:

- 1) objects without spectroscopic redshifts;
- 2) objects which had no the morphological type “radio galaxy”;
- 3) objects without NVSS observations.

³ Astronomical CATALOGS SUPPORT SYSTEM, (<http://cats.sao.ru>)

⁴ NASA/IPAC Extragalactic Database (<http://ned.ipac.caltech.edu>)

⁵ <http://www.sdss.org>

⁶ <https://vizier.u-strasbg.fr/viz-bin/VizieR>

Table 1. The basic radio catalogues used in the study

Catalog/Instrument*	Epoch	Frequency, GHz	Reference
TXS	1974–1983	0.365	Douglas et al. (1996)
GBIMO	1979–1996	2.5, 8.2	Lazio et al. (2001)
RCSP	1980–1981	3.9	Bursov et al. (1996)
GB6	1986–1987	4.8	Gregory et al. (1996)
PKS90	1989	8.4	Wright et al. (1991)
WENSS	1991	0.325, 0.609	Rengelink et al. (1997)
FIRST	1993–1994	1.4	Becker et al. (1994)
NVSS	1993–1996	1.4	Condon et al. (1998)
JVAS	1995–1997	8.4	Wrobel et al. (1998)
PMN Mi	1995–1996	0.96, 2.3, 3.9, 7.7, 11.2	Mingaliev et al. (1998)
SRCKi	1995–1996	0.96, 2.3, 3.9, 7.7, 11.2, 21.7	Kiikov et al. (2002)
KOV97	1997	0.96, 2.3, 3.9, 7.7, 11.2, 21.7	Kovalev et al. (1999)
VLSS	1998	0.074	Cohen et al. (2007)
NCPMi	1999	2.3, 3.9, 7.7, 11.2, 21.7	Mingaliev et al. (2001)
GPSra	2006–2010	1.1, 2.3, 4.8, 7.7, 11.2, 21.7	Mingaliev et al. (2012)
ATCA	2007	1.4	White et al. (2012)
CGR15	2008–2009	15	Richards et al. (2011)
BlMin	2005–2014	1.1, 2.3, 4.8, 7.7, 11.2, 21.7	Mingaliev et al. (2017)
GPSSt	2006–2017	1.1, 2.3, 4.8, 7.7/8.2, 11.2, 21.7	Sotnikova et al. (2019)
TGSS	2010–2012	0.15	Intema et al. (2017)
GLEAM	2013–2015	0.072–0.231	Hurley-Walker et al. (2017)
VLASS	2016–2019	2–4	Lacy et al. (2020)
RATAN-600	2017–2020	1.2, 2.3, 4.7, 8.2, 11.2, 22.3	Sotnikova et al. (2021)

* Names are given in accordance with the CATS identifiers

We performed an extensive scan of the literature including the optical, infrared, and radio surveys represented in the NED database, VizieR Information System, and CATS. To work with the NED database as well as with the VizieR collection of catalogues, the Python module `astroquery` was used (Ginsburg et al. 2019). It allows batch searches in a variety of databases using a common API⁷. In addition to the radio catalogues, cross-matching with WISE (Wright et al. 2010) was performed (see details in Section 6.2). The total number of the catalogs used is more than 170, the vast majority of the measurements are provided by 21 radio catalogues that are summarized in Table 1, where we include the epochs, frequencies of observations, and corresponding literature references. The data cover a time period of several dozens of years, and the main data are represented by the NRAO VLA Sky Survey (NVSS, Condon et al. 1998), Faint Images of the Radio Sky at Twenty-cm Survey (FIRST, Becker et al. 1994), Westerbork Northern Sky Survey (WENSS, Rengelink et al. 1997), Green Bank 6-cm Survey (GB6, Gregory et al. 1996), Australia Telescope 20 GHz Survey (ATCA20, Murphy et al. 2010), GaLactic and Extragalactic All-sky Murchison Widefield Array (GLEAM) survey at 72–231 MHz (2013–2014; Hurley-Walker et al. 2017), Giant Metrewave Radio Telescope Sky Survey (TGSS) at 150 MHz (2015; Intema et al. 2017), VLA measurements (Healey et al. 2007), and others. The time period begins in 1974 with the Texas Survey of Radio Sources, covering $-35^{\circ}5 < \delta < 71^{\circ}5$ at 365 MHz (TXS, Douglas et al. 1996; Gregory et al. 1996). A significant contribution in the measurements was provided by the Multiyear Monitoring Program of Compact Radio Sources at 2.5 and 8.2 GHz

(Lazio et al. 2001) and by the low frequency GLEAM⁸ survey at 72–231 MHz (Hurley-Walker et al. 2017). The multi-frequency quasi-simultaneous observations with the RATAN-600 radio telescope are presented by several catalogs at six frequencies from the papers of Bursov et al. (1996); Mingaliev et al. (1998); Kiikov et al. (2002); Kovalev et al. (1999); Mingaliev et al. (2001, 2017, 2012); Sotnikova et al. (2019, 2021).

The sample includes additional objects found in the literature individually. They are:

- NVSS J142047+120547 (Gabányi et al. 2021),
- NVSS J160608+312447 (Healey et al. 2008),
- RC J0311+0507 (Parijskij et al. 2014,
- NVSS J031147+050802),
- MRC 0251–273 (Miley & De Breuck 2008,
- NVSS J025316–270913),
- MRC 2025–218 (Miley & De Breuck 2008,
- NVSS J202759–214057), and
- MRC 2104–242 (Miley & De Breuck 2008,
- NVSS J210658–240504).

According to the early data (Sbarrato et al. 2015), NVSS J142047+120547 was classified as a beamed blazar source, but Gabányi et al. (2021) concluded from observations that it is most likely a young radio galaxy. For NVSS J160608+312447 there is no information in NED about the method for redshift determination; but as can be seen from Healey et al. (2008), the redshift was determined spectroscopically in the CGRaBS (Candidate Gamma-Ray Blazar Survey) survey, so we also added it to our sample.

⁷ <https://astroquery.readthedocs.io>

⁸ GaLactic and Extragalactic All-sky Murchison Widefield Array

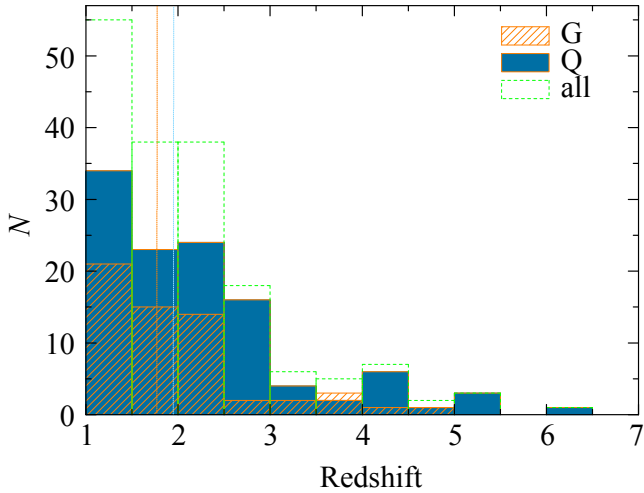


Figure 1. Redshift distribution for the sample. The median values are marked by the orange and blue lines for the G and Q types, respectively.

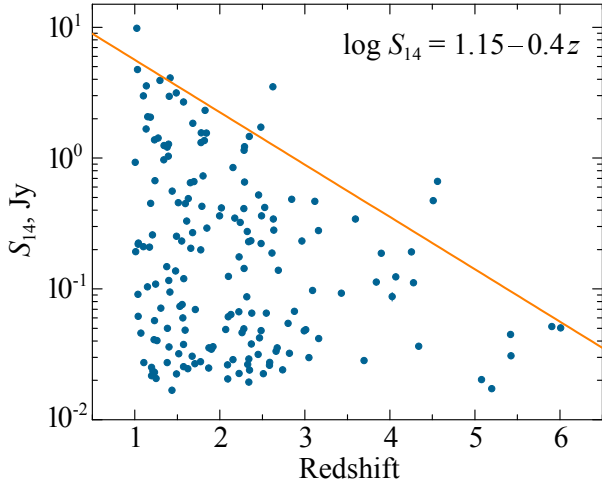


Figure 2. Flux density in Jy at 1.4 GHz versus redshift. The regression fit is drawn for the maximum fluxes inside bins with a redshift step of $\Delta z = 0.5$.

As a result, the sample contains 173 objects which are classified very diversely: 105 (61% of the sample) QSOs and QSO candidates, five BL Lacs, three BZQs, 59 radio galaxies and one object of mixed type (Table 2, a short fragment is presented. The full version can be found in VizieR⁹). For future analysis we consider two subsamples, one containing objects classified as galaxies with quasars (114 sources, named “Q”), and the rest 59 objects designated as “G”. The flux densities for the objects range from 0.02 to 9.8 Jy at 1.4 GHz with the median value of 0.12 Jy.

The redshifts of the galaxies extend from 1 up to 6.01 with median values of 1.78 for the G-type sources and 1.96 for the Q type (Fig. 1). The object with the highest redshift in our sample is J1225+4140, that is classified both as a galaxy and alternatively as a quasar, so we consider it as a Q-type source in our analysis. Its photometric redshift $z = 0.59 \pm$

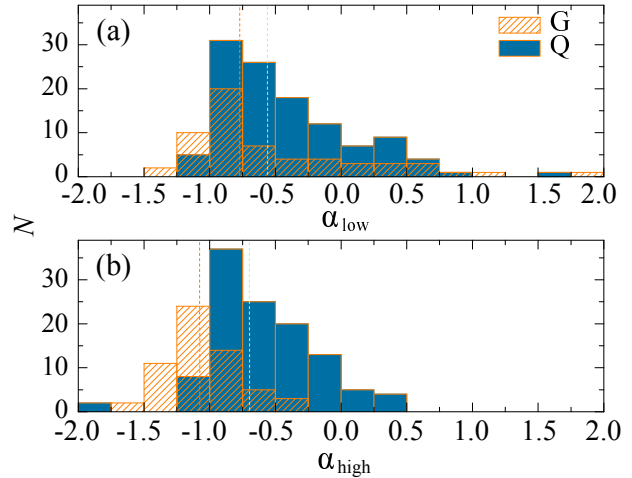


Figure 3. The low-frequency (panel a) and high-frequency (panel b) spectral index distributions for the G and Q source types. The median values are marked by the vertical dashed lines.

0.05, which strongly contradicts the spectroscopic redshift estimated in SDSS DR13¹¹ as $z = 6.008 \pm 0.001$. Its radio spectrum is well approximated with a straight line in the range from 150 MHz to 3 GHz and has a steep slope with $\alpha = -0.7$. We recently (in 2022–2023) estimated its flux density with RATAN-600 at frequencies higher than 3 GHz for the first time and obtained 19 ± 3 mJy at 4.7 GHz and 21 ± 5 mJy at 11.2 GHz (preliminary results to be published). These flux density values are in good agreement with its steep spectrum shape at 0.15–3 GHz.

In the “flux–redshift” diagram at 1.4 GHz (Fig. 2), an upper flux boundary, which gives the maximum luminosities of the observed radio galaxies at different redshifts, is presented. As it was supposed in Khabibullina & Verkhodanov (2009a), it could be due to the dynamics of cosmological expansion. Following the above mentioned authors, we fit a linear regression to the maximum values of the distribution in bins of $\Delta z = 0.5$. The regression relation is given by the formula $\log S_{1.4} = p + rz$, where $S_{1.4}$ is the flux density at 1.4 GHz, $p = 1.15$ is a constant intercept, and $r = -0.4$ is the slope of the line. The resulting regression is in good agreement with the regression obtained in Khabibullina & Verkhodanov (2009a). Here we point out the especially powerful radio galaxies whose fluxes are greater by more than half the value of the regression boundary: NVSS J043236+413829 (3C 119, $z = 1.023$) (Kellermann 1964), NVSS J074533+101112 (PKS 0742+10, $z = 2.624$) (Labiano et al. 2007), NVSS J160608+312447 (WISEA J160608.53+312446.5, $z = 4.56$, Gendre & Wall 2008), and NVSS J031147+050802 (4C+04.11, $z = 4.510$) (Gower et al. 1967).

3 RADIO PROPERTIES

3.1 Radio Spectra and Classification

We constructed broadband radio spectra of the galaxies (Fig. A1, Appendix) based on the results of cross identifica-

⁹ <https://cdsarc.cds.unistra.fr/viz-bin/cat/J/other/AstBu/78.443> ¹¹ http://www.sdss.org/dr13/data_access/bulk/

Table 2. The parameters of the galaxies in the sample: NVSS source name (J2000 format), redshift z , flux density at 1.4 GHz $S_{1.4}$ in Jy from the NVSS database, optical object type, and the literature where the optical classification was taken: [1]—Pâris et al. (2018); [2]—D’Abrusco et al. (2019); [3]—Souchay et al. (2015); [4]—Seymour et al. (2007); [5]—Stern et al. (1999); [6]—Sadler et al. (2019). The redshifts are taken from the NED database, SDSS database, and articles. A short fragment is presented.

NVSS name	z	$S_{1.4}$, Jy	Type	Reference
1	2	3	4	5
003005+295706	5.199	0.017 ± 0.001	G, QSO	SDSSdr13 ¹⁰
003205–041417	3.161	0.042 ± 0.002	G, QSO	[1]
003818+122731	1.395	1.034 ± 0.031	G, BL Lac	[2]
010152–283119	1.694	0.661 ± 0.020	G, QSO	[3]
011322+133505	2.661	0.033 ± 0.001	G, QSO	SDSSdr13
011651–205206	1.415	4.091 ± 0.123	G	[4]
011747+011407	3.696	0.028 ± 0.001	G, QSO	[1]
012229+192339	1.595	0.449 ± 0.014	G	[5]
012529+005407	1.711	0.070 ± 0.002	G, QSO	[1]
013028–261000	2.347	1.464 ± 0.049	G	[6]

Table 3. Spectral types in the sample

Type	Criteria	N	%
Peaked	$\alpha_{\text{low}} > 0, \alpha_{\text{high}} < 0$	31	17.9
Flat	$-0.5 \leq \alpha \leq 0$	28	16.2
Inverted	$\alpha > 0$	3	1.7
Upturn	$\alpha_{\text{low}} < 0, \alpha_{\text{high}} > 0$	6	3.5
Steep	$-1.1 < \alpha < -0.5$	81	46.8
Ultra-steep	$\alpha \leq -1.1$	23	13.3
Complex	Two or more maxima/minima	1	0.6

tion in the CATS database (within a $30'' \times 30''$ identification box), NED, and VizieR Information System. To exclude false field radio sources in the specified box, we used a technique of data analysis similar to that described by Verkhodanov et al. (2000b, 2009). The essence of the method is to use a joint analysis of the data in the coordinate and spectral spaces to separate out the probable identifications of specific radio sources at various radio frequencies. To this end, we use the *spg* program from the radio continuum data reduction package FADPS implemented at the RATAN-600 radio telescope (Verkhodanov 1997).

We performed a classification of spectral types based on the common criteria (e.g., Sadler et al. 2006; Tucci et al. 2008) listed in Table 3. The sample contains sources with a variety of spectral shapes. For the peaked and upturn shapes, the spectral indices α_{low} and α_{high} were calculated for the frequencies lower than or higher than the point where the spectral slope changes its sign from positive to negative or vice versa. For part of the spectra, the low-frequency spectral index matches with the high-frequency one.

Figure 3 shows the distribution of the low-frequency and high-frequency spectral indices for the two types of the sources. There is a clear difference in the distributions of the high-frequency spectral indices, where quasars demonstrate more flat spectral shapes, confirming their optical classification. The median values are $\alpha_{\text{low}} = -0.63$ and $\alpha_{\text{high}} = -0.83$ for the whole sample. For the subsample with galaxies (G) the median spectral indices are $\alpha_{\text{low}} = -0.77$, $\alpha_{\text{high}} = -1.08$, and for the Q subsample $\alpha_{\text{low}} = -0.56$, $\alpha_{\text{high}} = -0.69$ (Table 4). The two-colour diagram of the spectral indices in the

Table 4. The median and mean values of the spectral indices α_{low} and α_{high} for the G and Q source types. The standard deviations from the mean are given in parentheses. The last column shows the Pearson correlation coefficients for the “ $\alpha-z$ ” relation

Type	N	median	mean	r (p -value)
		α_{low}	$\alpha_{\text{low}} - z$	
G	59	-0.77	-0.52 (0.66)	-0.41 (0.001)
Q	114	-0.56	-0.41 (0.50)	0.22 (0.02)
		α_{high}	$\alpha_{\text{high}} - z$	
		-1.08	-1.05 (0.26)	-0.25 (0.06)
G	59	-0.69	-0.59 (0.39)	0.02 (0.58)
Q	114			

top panel of Fig. 4 presents the distribution of the spectral shapes of the sources. The point sizes correspond to the NVSS flux density level at 1.4 GHz.

The “ $\alpha-z$ ” diagram (Fig. 4b) shows the low-frequency (circles) and high-frequency (triangles) spectral indices relative to the redshifts in a wide range from 1 to 6. The blue and orange symbols represent the median spectral indices for redshift bins of 0.1 (for z from 1.0 to 2.5) and for bins of 0.5 (for z from 2.5 to 6). The distributions of α_{high} at redshifts from 1 to 3 and from 3 to 6 are significantly different (at the 0.05 level according to the Kolmogorov–Smirnov test), which is due to the deficiency of galaxies at $z > 3$. We did not find correlation between the redshift and the low-frequency and high-frequency indices; however, α_{low} and z does correlate when we examine the subsample of galaxies: $r = -0.41$ (p -value = 0.001). Other values for the “ $\alpha-z$ ” correlations are shown in Table 4.

We checked the “ $\alpha_{5-10}-z$ ” relation for the radio spectra recalculated into the rest frame using the $(1+z)$ correction (Fig. 5). The spectral index was estimated between frequencies 5–10 GHz. We do not find a correlation for the whole sample, as well as for the subsample of Q sources. But for the G-type sources, a significant anticorrelation was found (Pearson $r = -0.32$, p -value < 0.01).

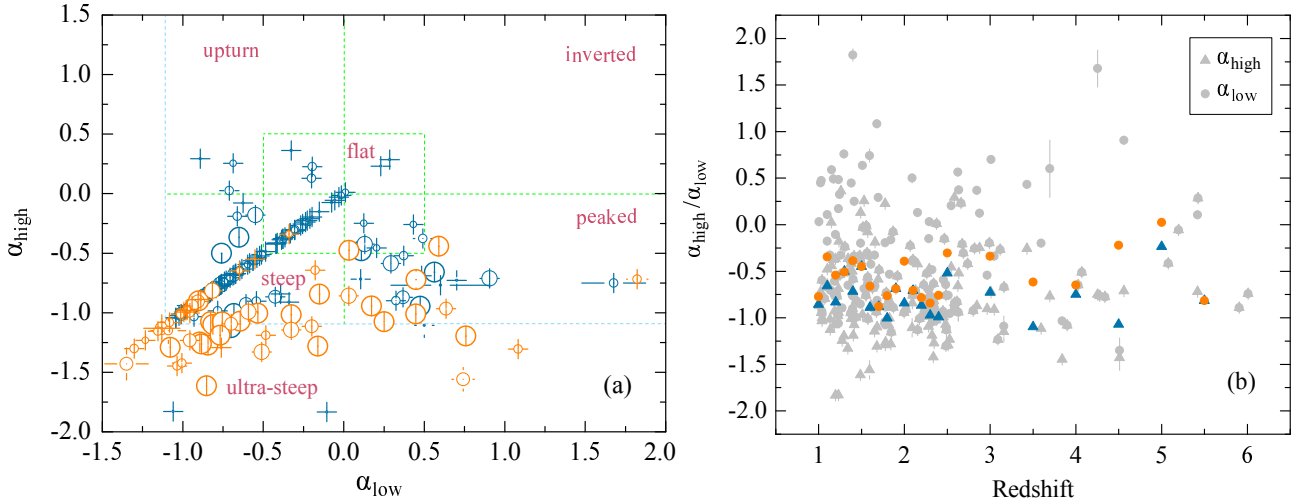


Figure 4. Panel (a): the “colour–colour” diagram for the spectral indices in our sample. The square shows the flat spectrum area, the green-coloured line indicates the area of ultra-steep spectrum sources. The point size is proportional to the NVSS flux density at 1.4 GHz. We show galaxies in orange and quasars in blue. Panel (b): the α versus z plot for low-frequency and high-frequency spectral indices. The colored symbols represent the median spectral indices for redshift bins of 0.1 (for z from 1.0 to 2.5) and 0.5 (for z from 2.5 to 5.5).

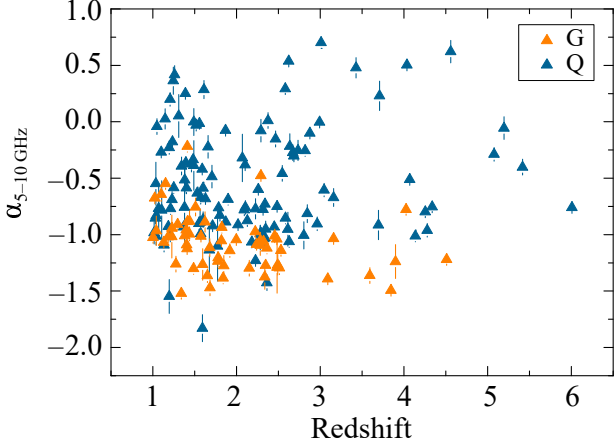


Figure 5. The α versus z plot for radio spectra in the sources rest frame for G and Q types separately.

3.2 The Average Spectrum

To study the population of distant galaxies, we used the continuum radio spectra averaged over the objects located within tight redshift intervals $\Delta z = 0.1$. The spectrum of each radio source was preliminarily recalculated into the rest frame using the $(1+z)$ correction. The detailed description of the average spectrum method is given in Verkhodanov et al. 2018; Sotnikova et al. 2021. As a result, we have calculated eighteen average spectra in the range $z = 1.0 – 3.1$ and the average radio spectrum for 21 galaxies at $z > 3.1$ (Fig. 6). The number of galaxies in each bin varies from 3 to 12, thus we can not conclude about cosmological evolution of the averaged spectra. We only note some of their characteristic features. Firstly, all the averaged spectra have a convex shape with flux density decrease with increasing frequency. The absolute value of the spectral index increases with increasing frequency (see

Table 5)¹². However, the spectral curvature is small, and only 4 spectra have peaks at frequencies above 100 MHz. Secondly, the spectral indices at 5 GHz and 11 GHz vary approximately from -0.6 to -1.0 , which means the optically thin emission. Thus, we do not detect prominent features of the spectral component related to a bright compact radio core.

3.3 Radio Luminosity

We calculated the radio luminosity at 5 GHz according to the common formula:

$$L_\nu = 4\pi D_L^2 \nu S_\nu (1+z)^{-\alpha-1}, \quad (1)$$

where ν is the frequency, S_ν is the measured flux density, z is the redshift, α is the spectral index, and D_L is the luminosity distance. We used the Λ CDM cosmology with $H_0 = 67.74 \text{ km s}^{-1} \text{ Mpc}^{-1}$, $\Omega_m = 0.3089$, and $\Omega_\Lambda = 0.6911$ (Planck Collaboration 2016) to estimate the luminosity distance.

Figure 7 shows the luminosity distribution with a median value of about $6.63 \times 10^{43} \text{ erg s}^{-1}$ and a mean of about $1.84 \times 10^{44} \text{ erg s}^{-1}$. The source NVSS J031147+050802 at $z = 4.51$ has the highest luminosity $L_{5\text{GHz}} \approx 2.17 \times 10^{45} \text{ erg s}^{-1}$. We note the bimodal character of the luminosity distribution: it is a superposition of two Gaussian distributions. This fact can be related to the sample heterogeneity. We constructed the radio luminosity distributions for the two subsamples: G and Q which have different distributions (Fig. 7).

The resulting bimodality of the total distribution is due to the bimodality of the Q group and approximately equal contribution of the G group. This group (G) has a peak in the distribution at the same luminosities as the second peak in the Q group (see also Table 6). The bimodal luminosity

¹² The average spectra were approximated by parabolas, and then we calculated the spectral index as a derivative at a given frequency.

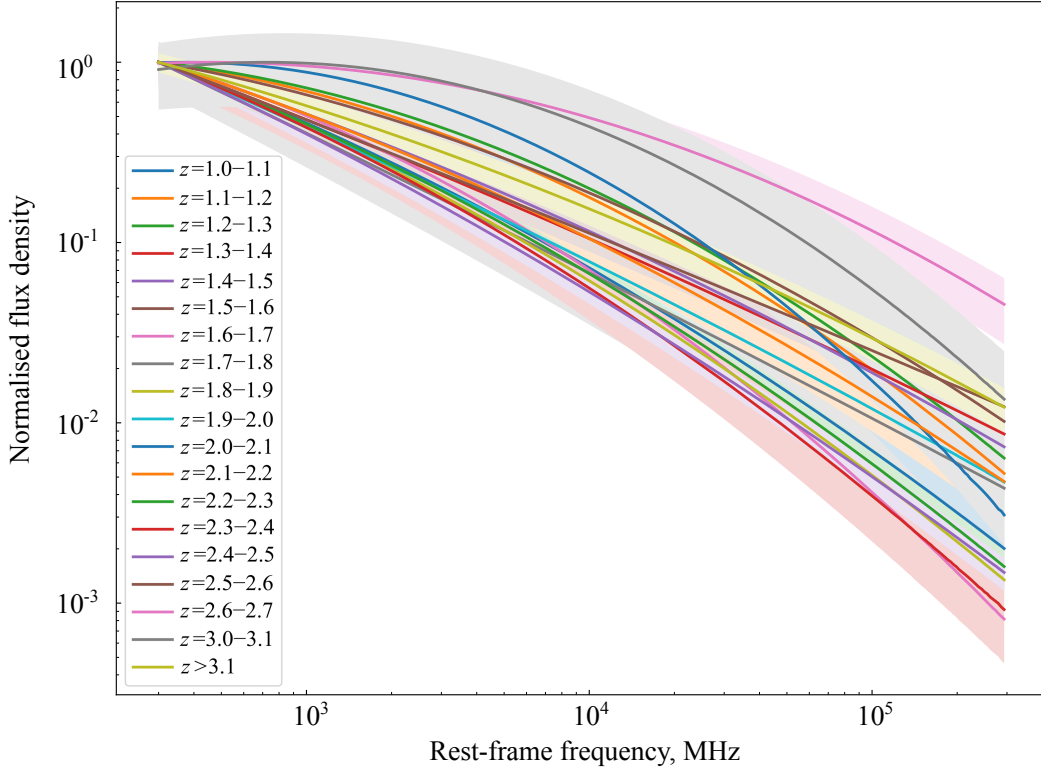


Figure 6. Average spectra of the sources normalised by the peak flux density. The colored lines relate to the redshift bins $z = 1.0 - 3.1$, and the corresponding strips represent the 3σ uncertainties.

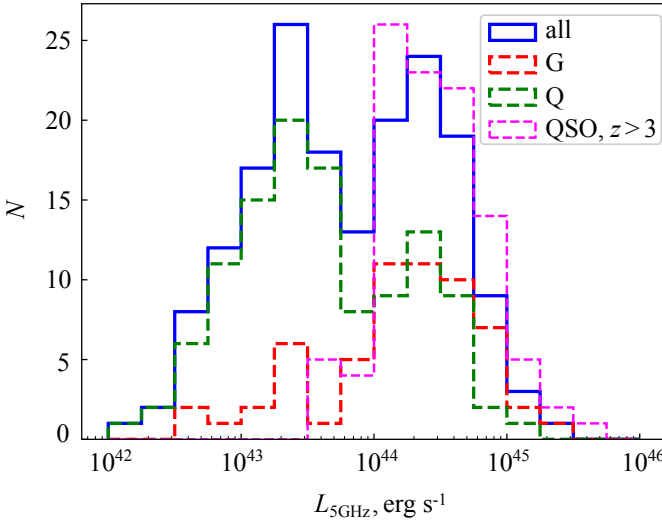


Figure 7. Distributions of the radio luminosity at 5 GHz. The radio luminosity distribution of distant quasars at $z > 3$ is marked in magenta (Sotnikova et al. 2021).

distribution of the Q group can mean that some objects from the Q group do not have prominent quasar properties and are misclassified.

Figure 8a presents a diagram of the luminosity at 5 GHz versus redshift. The empty bottom region is explained by the selection effect (the minimum flux density level at 1.4 GHz is limited to 20 mJy).

3.4 Radio Loudness

The more common radio loudness is defined as (Kellermann et al. 1989):

$$R = \frac{S_{5\text{GHz}}}{S_{4400\text{\AA}}} \quad (2)$$

where $S_{5\text{GHz}}$ is the rest-frame radio flux density at 5 GHz and $S_{4400\text{\AA}}$ is the rest-frame optical flux density at 4400 Å corresponding to the B or g filter.

Many authors suppose the same spectral indices for objects of the whole sample in estimating the rest-frame flux densities based on the observed flux densities in both the radio and optical bands. This assumption is often caused by a lack of knowledge about the spectral energy distribution. For example, Sotnikova et al. (2021) estimated the radio loudness for 102 high-redshift quasars based on broadband radio measurements; however, the authors took the same optical spectral index for all the sources. Here we calculated the radio loudness in two ways:

- 1) similarly to Sotnikova et al. (2021)—in this way we can compare the radio loudness for our sample and for the 102 high-redshift quasars;
- 2) the optical spectral index was calculated for each source based on the photometric data at 9134 Å (the SDSS z filter) and 3.4 μm ($W1$ band of WISE)—as the sources have redshifts greater than 1, the light emitted at a wavelength of 4400 Å is received in the region between z and $W1$, therefore this approach is more accurate.

The calculated values of radio loudness R_1 and R_2 versus redshift are shown in Figure 8b. Figure 9b presents the radio

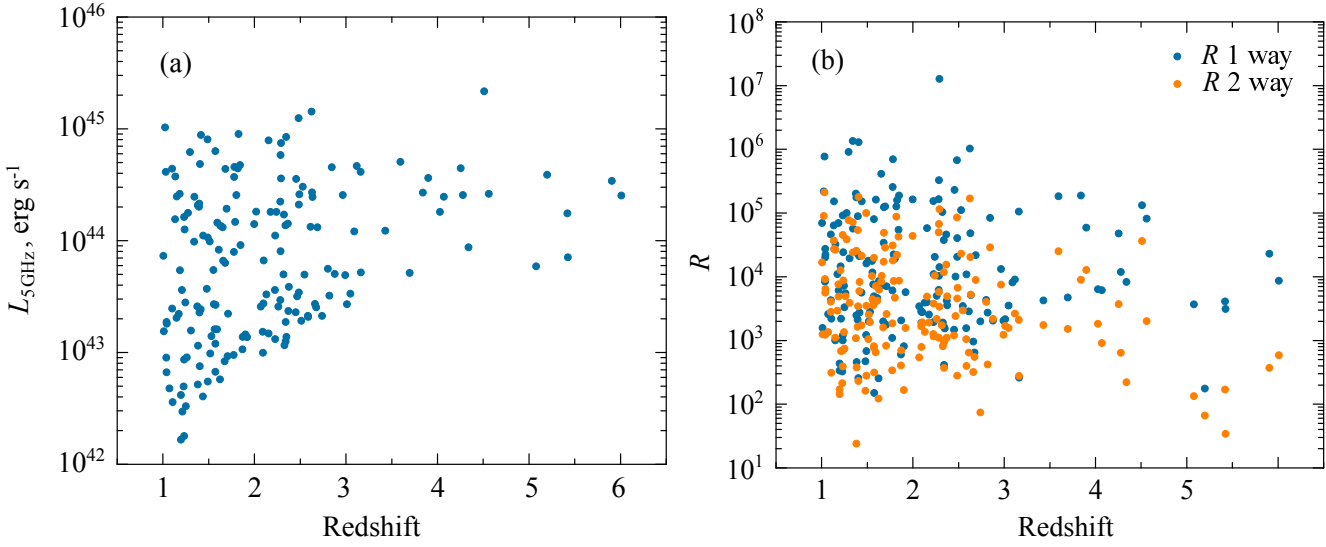


Figure 8. Luminosity at 5 GHz versus redshift (panel a) and radio loudness versus redshift (panel b). The blue and orange circles correspond to the radio loudness values calculated in two different ways.

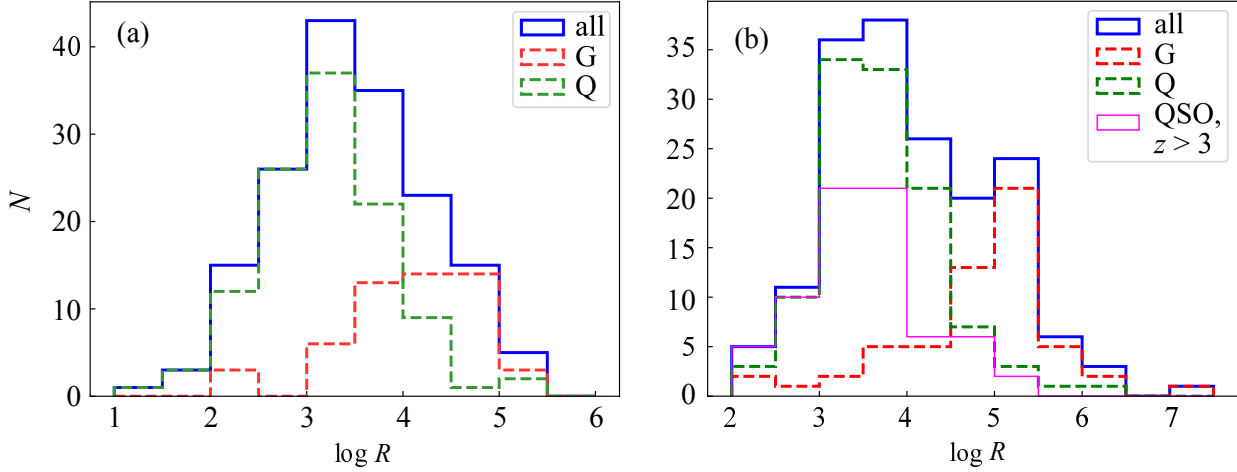


Figure 9. Distributions of the radio loudness. Panel a shows results obtained by second approach, panel b – by the first one. The radio loudness distribution of distant quasars at $z > 3$ is marked in magenta (Sotnikova et al. 2021).

loudness distribution which was estimated using the second approach, R_2 . The $\log R$ value spans from 1.38 to 5.33, the median is 3.41. The two subsamples (G and Q) have different radio loudness distributions with a more radio loud G group (see also Table 6).

4 RADIO VARIABILITY

Flux density variability over a time period of up to 30 years was estimated at 5 and 11 GHz using the variability (V_S) and modulation (M) indices (Aller et al. 1992; Kraus et al. 2003). The literature data were adopted within 10% ranges of these two frequencies. For example, at $\nu = 5$ GHz we used all data within 4.5–5.5 GHz. The median values of the number of measurements at 5 and 11 GHz over the sample are very small, $N_{\text{obs}} = 5$. The variability and modulation indices at 5 GHz and the number of observing epochs (N_{obs}) are

presented in Table 7 in columns (8)–(10) (A short fragment is presented. The full version can be found in VizieR¹³).

The number of observing epochs N_{obs} is an important parameter, which impacts the search for AGN variability. It is known that variability increases with the number of observations, which can be explained by the fact that peaks of variability are easily missed when sampling is very sparse (Tornikoski et al. 2000). We found a significant correlation (Fig. 10) between N_{obs} and the variability index at 5 GHz (Spearman $\rho = 0.43$, $p\text{-value} < 0.005$). The observations are not homogeneous and differ also in timescales, affecting the revealed variability level.

Table 8 lists the statistics of V_S and M . The negative variability indices were excluded from the calculations. We obtained the average variability and modulation indices for the sample to be 0.11–0.16 at 5 GHz and 0.14–0.18 at 11 GHz

¹³ <https://cdsarc.cds.unistra.fr/viz-bin/cat/J/other/AstBu/78.443>

Table 5. The peak frequency and the spectral indices at 5 GHz and 11 GHz for the average spectra of the galaxies from this work (top part) and for the average spectra of quasars from Sotnikova et al. (2021) (bottom part)

z	ν_{peak} , GHz	α_5	α_{11}
1.0–1.1	–	−0.84	−0.91
1.1–1.2	–	−0.66	−0.79
1.2–1.3	0.10	−0.63	−0.76
1.3–1.4	–	−0.67	−0.69
1.4–1.5	–	−0.68	−0.73
1.5–1.6	–	−0.60	−0.68
1.6–1.7	–	−0.93	−1.06
1.7–1.8	–	−0.78	−0.79
1.8–1.9	–	−0.90	−0.98
1.9–2.0	–	−0.76	−0.78
2.0–2.1	0.37	−0.68	−0.88
2.1–2.2	–	−0.72	−0.79
2.2–2.3	–	−0.88	−0.95
2.3–2.4	–	−0.95	−1.03
2.4–2.5	–	−0.91	−0.96
2.5–2.6	–	−0.63	−0.64
2.6–2.7	0.44	−0.36	−0.47
3.0–3.1	0.73	−0.46	−0.65
≥ 3.1	–	−0.60	−0.65
3.0–3.1	0.52	−0.21	−0.28
3.1–3.2	1.50	−0.19	−0.32
3.2–3.3	0.65	−0.26	−0.35
3.3–3.4	–	−0.36	−0.37
3.4–3.5	1.61	−0.23	−0.39
3.5–3.6	5.35	+0.03	−0.30
3.6–3.7	2.43	−0.12	−0.26
3.7–3.8	4.78	−0.01	−0.14
3.0–3.8	1.60	−0.18	−0.30

(Fig. 11, Table 8). The median V_{S_5} values for galaxies and quasars are 0.12 and 0.15, respectively (Fig. 12), but the distributions of both the variability and modulation indices for them are not significantly different (at the 0.05 level according to the Kolmogorov–Smirnov test). The most variable flux density is obtained for the galaxies with upturn, complex, inverted, and peaked spectra (Table 9).

Most radio sources have a quite low variability index, less than 0.25 (Fig. 13). Poor statistics for redshifts $z > 3$ does not allow us to find any difference in variability at different cosmological epochs.

5 PEAKED-SPECTRUM GALAXIES

We have found 31 galaxies (18%) having peaked radio spectra (PS). Among them 13 sources have already been known as GPS sources (Table 10, column (10)). All of them are bright radio sources with a flux density level about or more than 1 Jy in the GHz band. To classify the genuine HFP/GPS/MPS sources, the following common criteria are usually used: the observed peak frequency $\nu_{\text{obs,peak}}$ is less than 1 GHz for MPS and CSS sources, from 1 up to 5 GHz for GPS sources, and more than 5 GHz for HFPs; the spectral indices of the optically thick α_{thick} and thin α_{thin} emission parts are close to +0.5 and −0.7, respectively (for the peaked spectra they match with α_{low} and α_{high}); radio variability does not exceed 25% on a long timescale, as these objects are consid-

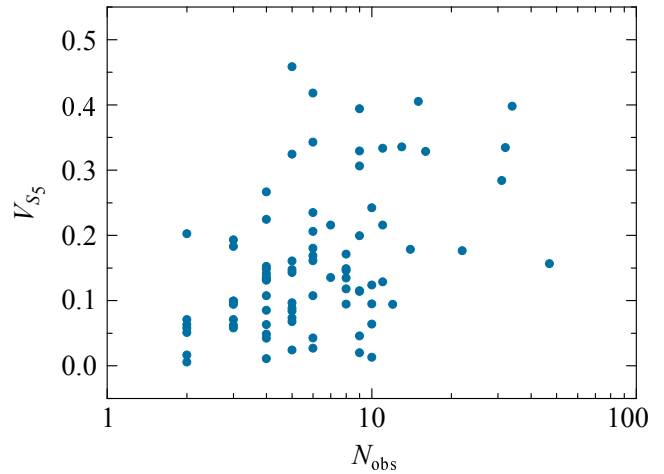


Figure 10. The variability index V_{S_5} versus the number of observations N_{obs} .

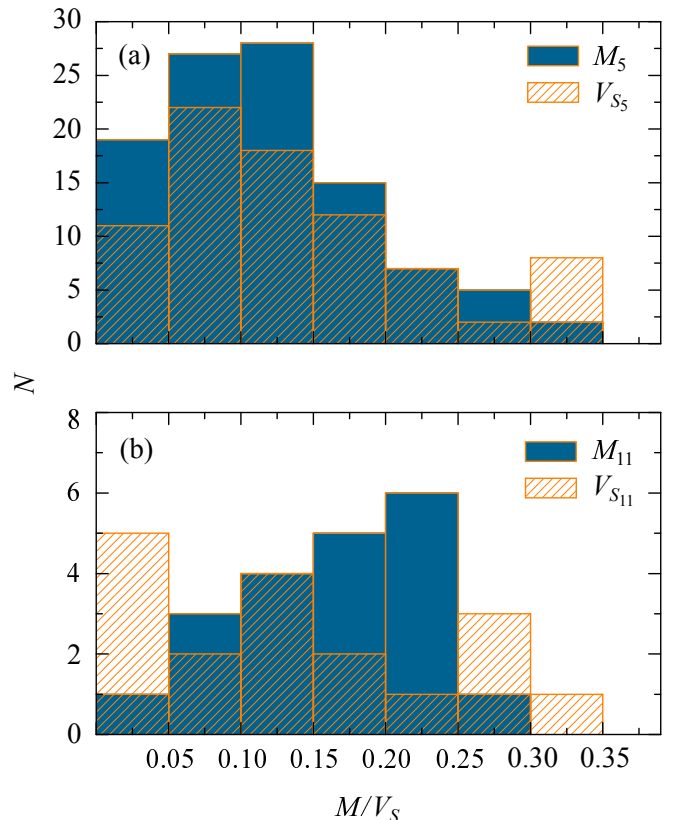


Figure 11. The distributions of the modulation M and variability V_S indices at 5 GHz (a) and 11 GHz (b).

ered as the least variable compact extragalactic radio sources (O’Dea et al. 1990, 1991; de Vries et al. 1997; O’Dea 1998; Edwards & Tingay 2004; O’Dea & Saikia 2021). MPS and CSS sources have different sizes, up to 1 kpc and about 20 kpc respectively. They are also located at different redshifts, MPSs at higher redshifts, $z > 1$ (Coppejans et al. 2016a), and CSS objects at closer distances.

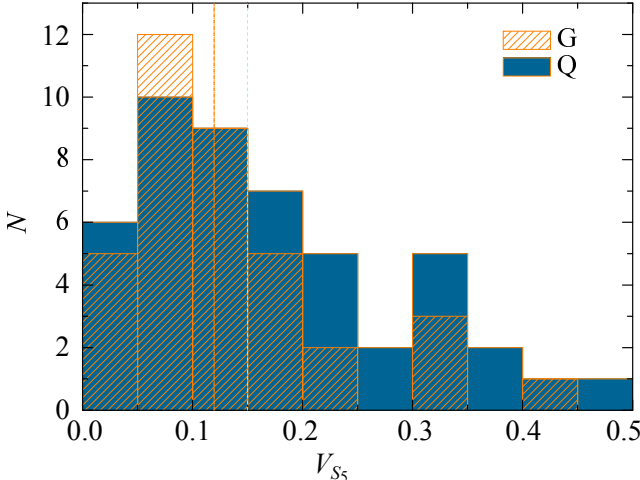
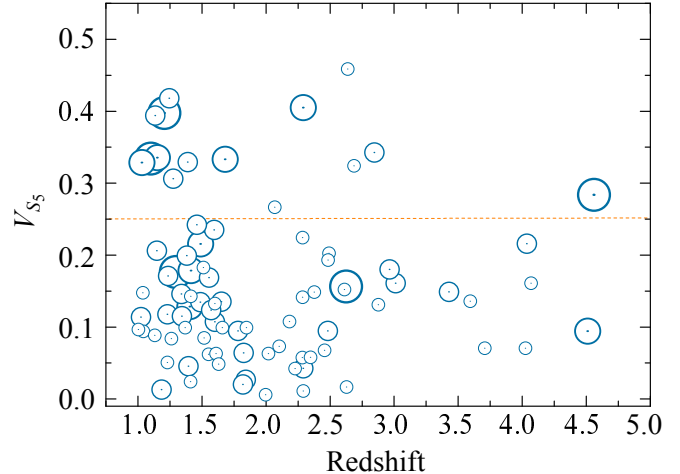
In our sample, among PS galaxies, there are two galaxies that are high frequency peaker (HFP) candidates, nine gigahertz-peaked spectrum (GPS) candidates, and 20 are

Table 6. Descriptive statistics of the radio luminosity and radio loudness in different subsamples

Subsample	$\log L_5, \text{erg s}^{-1}$			$\log R_1$			$\log R_2$		
	mean	sd	median	mean	sd	median	mean	sd	median
all (173)	43.81	0.69	43.82	4.06	0.92	3.92	3.48	0.81	3.41
G (59)	44.19	0.62	44.26	4.78	0.91	5.00	4.09	0.70	4.23
Q (114)	43.62	0.63	43.51	3.70	0.69	3.63	3.19	0.70	3.18
QSO, $z > 3$ (102)	44.45	0.38	44.37	3.56	0.69	3.49	—	—	—

Table 7. The sample parameters: source name at 2000.0 epoch, radio luminosity at 5 GHz L_5 , logarithm of radio loudness R , calculated in two ways, spectral indices α_{low} and α_{high} , radio spectrum type, modulation M and variability V indices at 5 GHz, number of observations N_{obs} , and the observed peak frequency in the spectrum $\nu_{\text{peak,obs}}$. A short fragment is presented.

Name, 2000.0	$\log L_5,$ erg s^{-1}	$\log R,$ 1 way	$\log R,$ 2 way	α_{low}	α_{high}	Sp. type	M_5	V_5	N_{obs}	$\nu_{\text{peak,obs}},$ GHz
1	2	3	4	5	6	7	8	9	10	11
J0030+2957	44.59 _{-0.01} ^{+0.01}	2.25 _{-0.01} ^{+0.01}	1.82 _{-0.37} ^{+0.37}	-0.06 ± 0.10	-0.06 ± 0.10	flat	—	—	—	—
J0032-0414	43.72 _{-0.06} ^{+0.05}	2.42 _{-0.06} ^{+0.05}	2.44 _{-0.28} ^{+0.17}	-0.67 ± 0.08	-0.67 ± 0.08	steep	—	—	—	—
J0038+1227	44.3 _{-0.05} ^{+0.04}	3.33 _{-0.05} ^{+0.04}	3.22 _{-0.11} ^{+0.08}	-0.76 ± 0.08	-0.50 ± 0.01	steep	0.09	0.05	9	—
J0101-2831	44.29 _{-0.05} ^{+0.05}	5.1 _{-0.12} ^{+0.1}	4.46 _{-0.12} ^{+0.09}	+0.29 ± 0.02	-0.59 ± 0.05	peaked	0.08	0.11	6	0.37
J0113+1335	43.43 _{-0.04} ^{+0.04}	2.98 _{-0.06} ^{+0.06}	2.51 _{-0.13} ^{+0.1}	+0.23 ± 0.13	+0.23 ± 0.13	inverted	0.15	0.07	3	—
J0116-2052	44.94 _{-0.02} ^{+0.02}	3.44 _{-0.09} ^{+0.07}	3.92 _{-0.04} ^{+0.04}	+0.25 ± 0.30	-1.08 ± 0.10	peaked	0.09	0.18	14	0.13
J0117+0114	43.71 _{-0.35} ^{+0.19}	3.67 _{-0.42} ^{+0.21}	3.18 _{-0.31} ^{+0.31}	+0.60 ± 3.08	-0.77 ± 0.04	peaked	—	—	—	0.11
J0122+1923	44.16 _{-0.04} ^{+0.08}	5.21 _{-0.21} ^{+0.2}	3.85 _{-0.34} ^{+0.34}	+0.74 ± 0.70	-1.56 ± 1.00	peaked	0.17	0.24	6	0.17
J0125+0054	43.35 _{-0.04} ^{+0.04}	3.85 _{-0.07} ^{+0.06}	3.41 _{-0.24} ^{+0.16}	-0.88 ± 0.02	-0.88 ± 0.02	steep	—	—	—	—
J0130-2610	44.93 _{-0.03} ^{+0.03}	—	—	-0.84 ± 0.02	-1.27 ± 0.05	ultra-steep	0.08	0.06	3	—

**Figure 12.** The distributions of the variability index V_{S5} for galaxies and quasars; the median values are equal to 0.12 and 0.15, respectively (dotted orange and blue lines).**Figure 13.** The redshift versus the variability index V_{S5} . Symbol sizes are proportional to N_{obs} and correspond to up to 5, 10, 20, and more number of observations.**Table 8.** The median, mean, maximum, and minimum values of the variability and modulation indices V_S and M

Parameter	N	Median	Mean	Min	Max
V_{S5}	85	0.13	0.16 ± 0.11	0.006	0.46
M_5	103	0.11	0.12 ± 0.07	0.002	0.33
V_{S11}	21	0.14	0.18 ± 0.14	0.02	0.47
M_{11}	24	0.17	0.16 ± 0.10	0.001	0.40

Table 9. The median and mean values of M_5 for different spectral types (standard deviations are given in parentheses)

Spectral type	N	Median	Mean
flat	15	0.10	0.11 (0.08)
peaked	25	0.14	0.15 (0.07)
steep, ultra-steep	54	0.09	0.10 (0.06)
upturn, complex, inverted	9	0.18	0.17 (0.09)

Table 10. The list of PS galaxies. Columns: (1) source name, (2) the spectral types in accordance with the turnover frequency, (3-4) the spectral indices α_{thin} and α_{thick} , (5) - the turnover frequency ν_{peak} calculated in the observer's frame of reference, (6) - the peak flux density S_{peak} , (7) - the variability index V_{S_5} , (8) - RA and Dec projected linear sizes, (9) - frequency on which projected linear sizes were calculated, (10) - the references to the galaxy size determination: [1]—Astrogeo database, [2]—An et al. (2022), [3]—Nesvadba et al. (2017), [4]—Callingham et al. (2017), [5]—Randall et al. (2011), [6]—O'Dea (1998), [7]—Spoelstra et al. (1985), [8]—O'Dea et al. (1991), [9]—Snellen et al. (2002), [10]—Sanghera et al. (1995)

Name	sp. type	α_{thin}	α_{thick}	$\nu_{\text{peak}},$ GHz	$S_{\text{peak}},$ Jy	V_{S_5}	LS, kpc	Frequency, GHz	Reference
1	2	3	4	5	6	7	8	9	10
J0101–2831	MPS	-0.77 ± 0.05	$+0.35 \pm 0.04$	0.27 ± 0.01	1.07 ± 0.02	0.11	0.022×0.052	8.7	[1], [4]
J0116–2052	MPS	-1.04 ± 0.04	$+0.10 \pm 0.04$	0.08 ± 0.01	13.36 ± 0.09	0.18	0.358×0.152	8.7	[1], [4,5]
J0117+0114	MPS	-0.76 ± 0.10	$+5.61 \pm 0.28$	0.11 ± 0.01	0.18 ± 0.01	—	—	—	—
J0122+1923	MPS	-0.83 ± 0.08	$+1.05 \pm 0.28$	0.17 ± 0.01	1.38 ± 0.03	0.24	0.133×0.800	8.7	[1], [4]
J0148+1028	MPS	-1.20 ± 0.11	$+0.41 \pm 0.06$	0.32 ± 0.02	1.05 ± 0.03	0.34	0.130×0.152	8.7	[1], [4]
J0232–0742	MPS	-0.46 ± 0.37	$+1.37 \pm 2.48$	0.17 ± 0.06	0.09 ± 0.01	—	—	—	—
J0432+4138	MPS	-0.72 ± 0.02	$+0.25 \pm 0.06$	0.16 ± 0.02	17.62 ± 0.24	0.11	0.340×0.059	8.7	[1], [6]
J0745+1011	GPS	-0.99 ± 0.03	$+0.44 \pm 0.02$	2.31 ± 0.04	4.17 ± 0.02	0.16	0.039×0.075	7.6	[7]
J0837–1951	MPS	-1.11 ± 0.04	$+0.66 \pm 0.04$	0.34 ± 0.01	11.15 ± 0.13	0.33	0.160×0.320	7.6	[1], [4]
J0904+4727	GPS	-0.57 ± 0.56	$+0.72 \pm 0.64$	1.68 ± 0.54	0.22 ± 0.02	0.22	0.073×0.073	4.8	[1]
J0909+4753	MPS	-0.53 ± 0.16	$+0.56 \pm 0.37$	0.53 ± 0.07	0.31 ± 0.02	0.46	0.058×0.054	8.7	[1]
J1002+0158	MPS	$-2.60 \pm -$	$+0.33 \pm -$	$1.42 \pm -$	$0.03 \pm -$	—	—	—	—
J1109+3744	MPS	-0.53 ± 0.07	$+0.71 \pm 0.45$	0.50 ± 0.06	1.45 ± 0.06	0.41	0.086×0.138	7.6	[1]
J1126+3345	MPS	-1.30 ± 0.08	$+0.26 \pm 0.05$	0.24 ± 0.01	3.57 ± 0.06	0.12	0.025×0.071	7.6	[1]
J1129+5025	MPS	-0.89 ± 0.08	$+0.52 \pm 0.43$	0.06 ± 0.01	7.23 ± 0.18	0.10	0.061×0.168	7.6	[1]
J1133+2936	MPS	-0.75 ± 0.04	$+5.49 \pm 0.08$	0.09 ± 0.01	1.30 ± 0.03	—	—	—	—
J1232+6644	GPS	-0.68 ± 0.13	$+6.42 \pm 0.55$	0.51 ± 0.01	0.10 ± 0.03	0.05	—	—	—
J1438+0150	MPS	-0.89 ± 0.09	$+7.73 \pm 0.01$	0.09 ± 0.01	0.83 ± 0.03	—	—	—	—
J1459+4442	HFP	-0.77 ± 0.21	$+0.35 \pm 0.06$	7.58 ± 0.55	0.21 ± 0.01	0.15	0.058×0.042	8.7	[1]
J1521+0430	GPS	-1.47 ± 0.08	$+0.50 \pm 0.04$	0.84 ± 0.03	4.77 ± 0.11	0.18	0.047×0.076	8.7	[1], [8]
J1541+3840	GPS	-0.82 ± 0.18	$+0.35 \pm 0.18$	0.74 ± 0.09	0.07 ± 0.01	—	—	—	—
J1545+4130	GPS	-0.17 ± 0.03	$+3.11 \pm 1.66$	0.37 ± 0.11	0.09 ± 0.01	0.13	0.041×0.100	7.6	[1]
J1550+4536	GPS	-1.97 ± 0.39	$+0.35 \pm 0.06$	5.21 ± 0.63	0.07 ± 0.01	0.16	0.032×0.062	7.6	[1]
J1602+3326	GPS	-0.64 ± 0.05	$+0.20 \pm 0.05$	0.70 ± 0.06	2.79 ± 0.06	0.33	0.114×0.033	7.6	[1], [8]
J1606+3124	GPS	-0.84 ± 0.09	$+0.33 \pm 0.10$	2.43 ± 0.16	0.73 ± 0.02	0.31	0.056	8.4	[2], [8]
J1640+1220	MPS	-0.69 ± 0.07	$+0.01 \pm 0.09$	0.07 ± 0.42	4.05 ± 2.28	0.34	0.090×0.073	7.6	[1], [9]
J2037–0010	MPS	-0.98 ± 0.22	$+0.93 \pm 0.24$	0.38 ± 0.04	0.92 ± 0.09	0.18	—	—	—
J2058+0542	MPS	-0.97 ± 0.02	$+0.73 \pm 0.05$	0.27 ± 0.01	2.89 ± 0.04	0.20	0.126×0.337	7.6	[1], [9]
J2227–2705	MPS	-0.96 ± 0.07	$+1.09 \pm 0.17$	0.17 ± 0.01	1.42 ± 0.01	—	3.3	$4.8/8.4^a$	[3], [4]
J2250+7129	MPS	-1.13 ± 0.06	$+0.12 \pm 0.05$	0.05 ± 0.01	13.93 ± 0.49	0.03	0.100×0.173	7.6	[1], [10]
J2307+1450	HFP	-3.42 ± 1.37	$+0.40 \pm 0.10$	7.24 ± 1.46	0.22 ± 0.01	0.42	0.025×0.061	7.6	[1]

^a VLA measurements

MPS candidates. The variability index V_{S_5} was estimated for 24 PS galaxies, and it varies from 0.05 to 0.46. For eight of them the variability level higher than 0.25 at 5 GHz.

The projected linear sizes of the PS galaxies are shown in Table 10 (column (8)). The data for two of them, J1606+3124 and J2227–2705, were taken from the literature. For 20 sources we estimated the linear sizes using the publicly available images in the Astrogeo database¹⁴ at 7.6 and 8.7 GHz, because these are the frequencies available for most of our sources. For nine sources the linear sizes have not been estimated. The sizes span from 0.022 to 0.8 kpc, the median is 0.073 kpc, excluding the size of J2227–2705 that was estimated based on a lower-resolution VLA image.

We found eleven new MPS, five new GPS, and two new HFP candidates. The objects are compact, but the radio spectra of most new PS galaxies are not well determined due to poor radio data at frequencies greater than several GHz, where larger radio variability of AGNs is expected than in

the MHz domain. Taking into account that we analyze the data from many telescopes with different angular resolutions and systematic errors, multi-frequency and long-term radio measurements are needed for reliable classification of their radio spectra.

It is clearly seen that there are almost no HFP galaxies in the sample. Even the sources with inverted or upturn radio spectra can be HFP candidates for which there are no high-frequency measurements, they also make up a small fraction, about 6%, of galaxies in the sample (Table 3). One of the possible reasons for the absence of HFPs in the sample of bright radio galaxies can be the selection method that was used for sample construction. A relatively low frequency of the source selection (1.4 GHz) could lead to missing of the inverted spectrum sources which had a flux density less than 20 mJy at MHz frequencies.

We fitted peaked spectra of PS galaxies with a function that describes synchrotron self absorption (SSA) radiation emitted by electrons with the power-law energy distribution in a homogeneous magnetic field (Pacholczyk 1970;

¹⁴ <http://astrogeo.org>

Türler et al. 1999):

$$S_\nu = S_{\text{peak}} \left(\frac{\nu}{\nu_{\text{peak}}} \right)^{\alpha_{\text{thick}}} \times \frac{1 - \exp(-\tau_m(\nu/\nu_{\text{peak}})^{\alpha_{\text{thin}} - \alpha_{\text{thick}}})}{1 - \exp(-\tau_m)}, \quad (3)$$

where $\tau_m \approx \frac{3}{2} \left(\sqrt{1 - \frac{8\alpha_{\text{thin}}}{3\alpha_{\text{thick}}}} - 1 \right)$; ν_{peak} is the turnover frequency; S_{peak} is the maximum flux density at the turnover frequency; α_{thin} and α_{thick} are the spectral indices of the optically thin and thick parts of the spectrum; τ_m is the optical depth at the turnover. The fitted parameters for the peaked spectra are presented in Table 10 (columns (3)–(6)). Most of these spectra are well described with $0.25 < \alpha_{\text{thick}} < 0.75$ and $-0.40 < \alpha_{\text{thin}} < -1.20$. Three sources (J0745+1011, J1521+0430, J1606+3124) have an upturn component in their spectra below 1 GHz. Optically thin part of the spectra has cut-off and requires an additional absorption for J0122+1923 above 9 GHz and for J2227–2705 above 2 GHz.

6 DISCUSSION

The obtained radio parameters for the sample are summarised in Table 7: radio luminosity at 5 GHz, logarithm of radio loudness, calculated using two approaches, spectral indices α_{low} and α_{high} , radio spectrum type, and the observed peak frequency in the spectrum. Below we discuss the dichotomy of the sources' types in the sample, mid-IR properties and classification, PS galaxies, and variability characteristics.

6.1 Distant Galaxies vs Distant Quasars

Sotnikova et al. 2021 studied the radio properties of 102 distant quasars at redshifts $z \geq 3$. Here we compare their characteristic radio features with similar properties of distant galaxies. We note that these samples have different spectral type distributions: among quasars at $z \geq 3$ prevail objects with the peaked and flat (70% of the sample) radio spectra and only 15% of the objects have steep spectra. At the same time, the galaxies mainly have steep and ultra steep radio spectra (60% of the sample), and 33% have peaked and flat radio spectra in total. These differences mean the dominating contribution of the compact bright radio core in the total spectrum for the quasars, while the radio core is less pronounced for the galaxies. The constructed average spectra well demonstrate the different spectral behavior for both samples. Firstly, the different values of the spectral index: the galaxies have steep ones, while the quasars have flat indices (Table 5). Secondly, the average quasar spectra have peaks varying from 0.5 GHz to 5.4 GHz (Table 5), while we do not reveal the peak in the average spectra of the galaxies, except for four cases.

Figure 7 shows the radio luminosity distributions for distant galaxies and distant quasars. The statistical properties of these distributions are presented in Table 6. We note that distant quasars have a similar radio luminosity distribution as the subsample G (and the high luminosity subgroup of

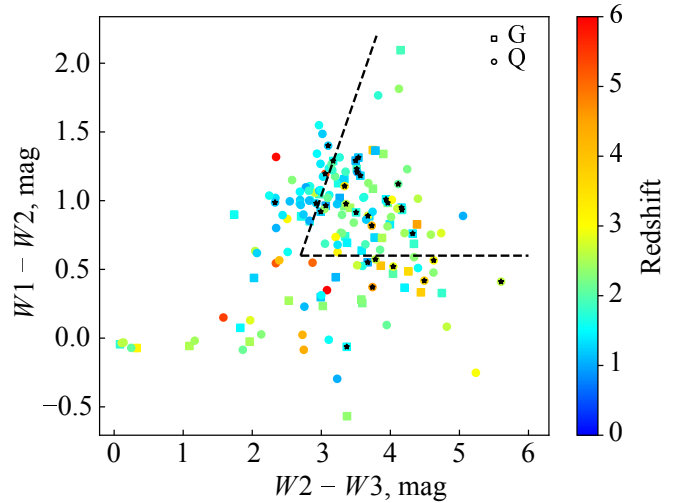


Figure 14. The WISE ‘color–color’ diagram for our sample. The sources are colored according to their redshift. The dashed lines show the region for high-redshift objects Stern et al. (2005); Krogager et al. (2018). Black stars are the MPS objects.

the Q subsample). This fact can be explained by the selection effect: at high redshifts more bright quasars are detected easier.

We calculated the radio loudness using the first approach (the same optical spectral index for all the sources) to compare with quasars at $z \geq 3$. Figure 9a demonstrates that the radio loudness distributions of distant quasars and the Q subsample are similar (see also Table 6). It is an expected result if the distant quasars and the Q subsample belong to the same kind of the sources with a continuous distribution of radio properties. At the same time, the distant quasars have lower radio loudness compared to the group G. This fact is expected, because quasars are usually brighter compared to radio galaxies in the optical band.

6.2 WISE Color Diagrams

We searched for the mid-IR counterparts in the Wide-field Infrared Survey Explorer (WISE, Wright et al. 2010) all-sky catalog for all the sources in our sample. We cross-matched the sources' positions with the WISE source catalog by adopting a search radius of $20''$. For each source with several counterparts in the WISE catalog located within the aforementioned area, the object nearest to the coordinates was selected.

Figure 14 shows the WISE ‘color–color’ diagram for the sample ($W_1 - W_2$ vs $W_2 - W_3$, where W_1 , W_2 , and W_3 are the WISE magnitudes at effective wavelengths of 3.4, 4.6, and $12 \mu\text{m}$). The G and Q subsamples are marked by squares and circles respectively. The sources are colored according to their redshifts. The MPS objects are marked as black stars.

As expected, the Q population is faint ($W_1 > 15$) and red in the $W_1 - W_2$ color. The G population has a medium $W_1 - W_2$ color of 0.8.

In the paper of Krogager et al. (2018), Fig. 2 demonstrates the WISE ‘color–color’ diagram of radio sources that have been identified as quasars in the SDSS spectroscopic catalog. To separate low-redshift quasars,

the authors applied the following photometric cut: $W1 - W2 < 1.3$ ($W2 - W3$) – 3.04 and $W1 - W2 > 0.6$.

We depicted the same region in Fig. 14 (where dashed black line shows the region of color-space where high-redshift objects can be found). As expected (Lacy et al. 2004; Stern et al. 2005; Krogager et al. 2018), the Q subsample at $z > 2$ dominates there (73% of the sources in that region). In the same area there are relatively many objects with lower redshifts ($1 < z < 2$), which is most likely due to the incompleteness of the sample. The fact that almost all MPS objects are located in the designated area confirms that these objects are distant.

Figure 15 shows the WISE "color-color" diagrams for our sample and the sample of bright quasars at $z \geq 3$ from Sotnikova et al. (2021) for comparison. The signatures indicate areas of different object types. By comparing the two panels of Fig. 15, we reveal the wider distribution of IR properties for the galaxies from the sample. Despite the fact that the two samples are incomplete and different, it is clear that the collected list of the galaxies is heterogeneous and contains different types of AGNs.

It is unavoidable that a certain number of objects would drop out of their area. With the orange line, we marked the "AGN" region, which includes the WISE QSOs and Seyfert galaxies (Jarrett et al. 2011): $W2 - W3 > 2.2$ and $W2 - W3 < 4.2$, $W1 - W2 > (0.1 \times (W2 - W3) + 0.38)$ and $W1 - W2 < 1.7$.

Fifty-four percent of our objects, including most of the MPSs, lie within this box. Most of the studied objects are located in the WISE QSO area above $W1 - W2 = 0.8$ (Stern et al. 2012) (Fig. 15a).

6.3 PS Population at High Redshifts

We found 31 (18%) galaxies with peaked radio spectra, which is significantly less than in the samples of bright distant quasars at $z \geq 3$ in Sotnikova et al. (2021), where peaked spectrum sources accounted for 46% of the sample. Still, it is larger than in some mixed galaxy and quasar samples: for example, O'Dea (1990) found about a 10% fraction of PS sources. A small fraction, not more than 10%, of radio sources in the 1 Jy complete sample (Planck Collaboration et al. 2011), showed peaked spectra, and they were mostly identified as blazars. In Mingaliev et al. (2013), the authors obtained only several per cents of sources with a constant peaked spectrum shape over a long period of time. Among 5890 radio sources from the complete sample of the AT20G survey with a flux density more than 40 mJy, 21% of the sources were found to have peaked spectra (Murphy et al. 2010).

Most of the PS galaxies in the sample under investigation are MPS candidates (20). Their redshifts and small linear sizes corresponding to the generally accepted MPS conception allow us to consider all the 20 galaxies with $\nu_{\text{peak,obs}} < 1$ GHz as MPS candidates. The median value of their redshift is 1.6. For reliable classification of all PS types in the sample, we need simultaneous multi-frequency radio data to define the turnover, preferably at several epochs, and long-term monitoring at several frequencies to determine whether there is variability at any or all of the frequencies.

The discovered peaked spectrum quasars are located at higher redshifts than quasars with other types of spectra.

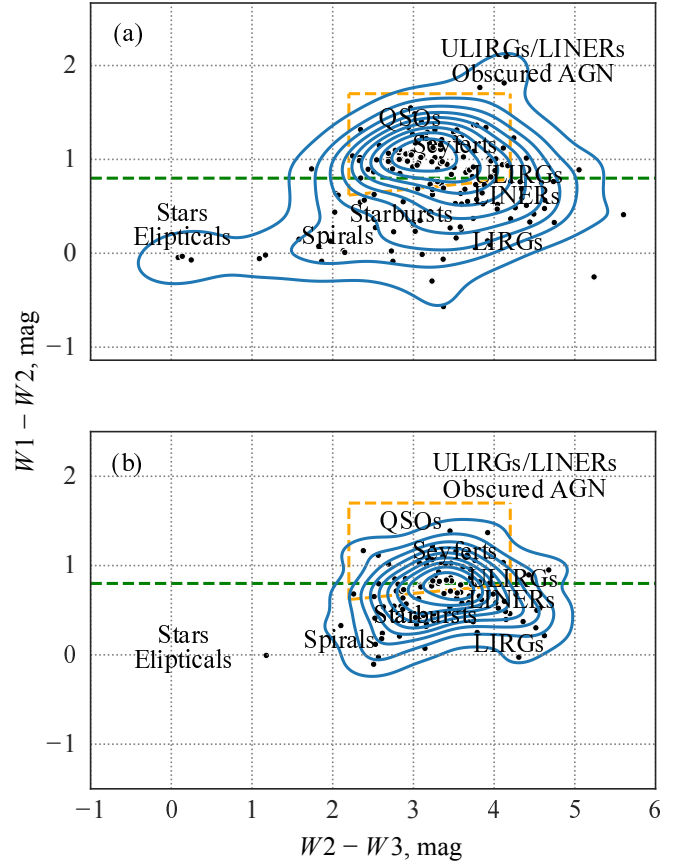


Figure 15. Panel (a): the WISE color diagram of our sample. Panel (b): the WISE color diagram for the bright quasars at $z \geq 3$ from Sotnikova et al. (2021). The green dashed line ($W1 - W2 = 0.8$) is the threshold above which QSOs are expected (Stern et al. 2012). The orange dashed line is the "AGN box" Jarrett et al. (2011).

There are 18 PS quasars in the sample with the average $\langle z \rangle = 2.74$ and the remaining 96 QSOs have $\langle z \rangle = 1.83$. That confirms the plausibility of searching for young and high-redshift AGNs among the MPS sources (see, for example, Coppejans et al. (2015)). However, the same is not true for the galaxies.

7 SUMMARY

We have collected a sample of 173 bright HzRGs in the radio domain ($S_{1.4} \geq 20$ mJy) at redshifts $z \geq 1$ for the study. Using available literature measurements in a wide frequency range (74 MHz–22 GHz) on a time scale of 30 years, we have constructed radio spectra of the galaxies and determined their types, classifying the most of them as having a steep or ultra-steep radio spectrum (60% of the sample). The spectral indices calculated at low and high frequencies vary on average from –0.6 to –1, the median values are $\alpha_{\text{low}} = -0.77$ for the galaxies not identified with quasars and $\alpha_{\text{low}} = -0.56$ for the galaxies with quasars (Section 3.1). The median spectral index for the entire sample $\alpha_{\text{low}} = -0.63$ agrees well with the previous studies (e.g., Mauch et al. 2013; Ramasawmy et al. 2021). In comparison with the spectral indices of the radio sources in the revised 3C catalogue (Kellermann et al.

1969), where $\alpha_{0.75-5} = -0.85$ was obtained for galaxies and $\alpha_{0.75-5} = -0.79$ for quasars, we derived a similar slope for the galaxies and more flat spectra for the quasars at low frequencies α_{low} (0.10–7.4 GHz).

We classified about 18% (31) of spectra as PS with predominant MPS type (20/31). Most of them fall into the high-redshift AGN box in the WISE color space diagram.

For the whole sample we have not found the evolution of radio spectra with redshift, the so called “ $\alpha-z$ ” correlation, when more distant galaxies have steeper radio spectra; but suspecting the influence of quasars in our sample, we checked that relation for 59 galaxies not identified with quasars and blazars. In that case there exists, indeed, a significant anticorrelation between α_{low} and z , and also between α_{5-10} calculated with k-correction at the rest-frame frequencies of 5–10 GHz and z , as it was reported in the previous studies (e.g., Miley & De Breuck 2008; Afonso et al. 2011).

The obtained spectral indices at frequencies of 1–10 GHz in the observer’s frame of reference indicate optically thin radiation in the frequency range of 2–30 GHz in the source’s reference frame for most of the objects. Sixteen per cent of the sample objects are characterized by a flat radio spectrum typical of the compact core emission in quasars. There is a systematic flattening of the spectrum at low frequencies (5 GHz) relative to the high frequencies (11 GHz). We assume that this is explained by the synchrotron self-absorption mechanism, a model of which explains fairly well the radio spectra shapes for the majority of the PS galaxies in our sample (Section 5).

An analysis of the modulation and variability indices has shown that the median variability at 11 GHz is higher than at 5 GHz. Since the radio spectra of most objects (78%) tend to steepen toward high frequencies (i.e., at higher frequencies the flux density decreases), we assume that this causes a selection bias leading to the detection of sources with higher variability amplitude at higher frequencies. The median values of the flux density variability index are $V_{S11}=0.14$ and $V_{S5}=0.13$, which generally indicates a weak or moderate character of the long-term variability of the studied galaxies. Several blazars included in the sample demonstrate variability up to 50%, but most of the quasars, AGNs, and blazars in the sample exhibit moderate variability of about 20%, which is the typical value for galaxies with AGNs and quasars at lower redshifts (Fan et al. 2007). Our work has shown that the variability of bright radio galaxies at large redshifts, up to $z=5$, does not differ significantly from the variability of galaxies at $z<1$ (having characteristic values of 10–20%), being caused by presumably similar physical phenomena in the galaxy centers, namely the processes around a massive central object, i.e., emission of the relativistic jet and the repercussions of its propagation through the interstellar medium. For the AGN, such moderate variability on scales of tens of years presumably occurs in the radio core itself (e.g., Marscher et al. 2008). In order to clarify the processes and localization of the radio emission source in each specific case, an analysis of simultaneous measurements at several frequencies and the evolution of the radio spectrum is essential.

Selection of bright and distant radio galaxies using the NASA/IPAC Extragalactic Database (NED) revealed that the sample includes objects classified in a fairly wide range: from subclasses of blazars and AGNs to QSOs. We found that our sample has a very high rate of identification with

quasars (114 of 173 objects). The scattering of the obtained characteristics (radio spectrum types, radio luminosity values, variability amplitudes, dispersion in the WISE colour diagram) confirms the diversity of radio emission sources in such galaxies.

ACKNOWLEDGEMENTS

A part of the observed data was obtained with the RATAN-600 scientific facility. This research has made use of the NASA/IPAC Extragalactic Database (NED), which is operated by the Jet Propulsion Laboratory, California Institute of Technology, under contract with the National Aeronautics and Space Administration; the CATS data base, available on the Special Astrophysical Observatory website.

FUNDING

The work was performed as part of the SAO RAS government contract approved by the Ministry of Science and Higher Education of the Russian Federation.

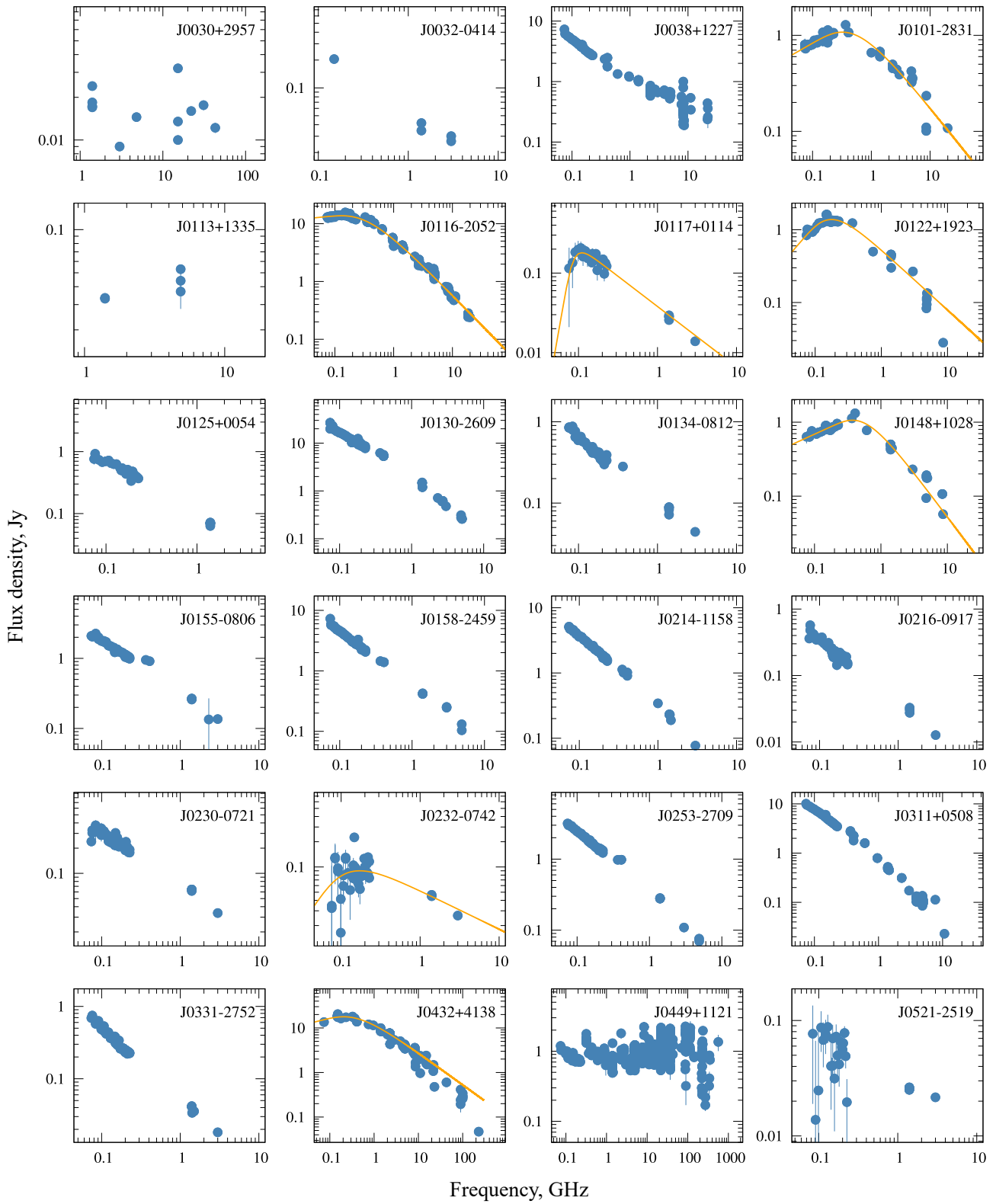
REFERENCES

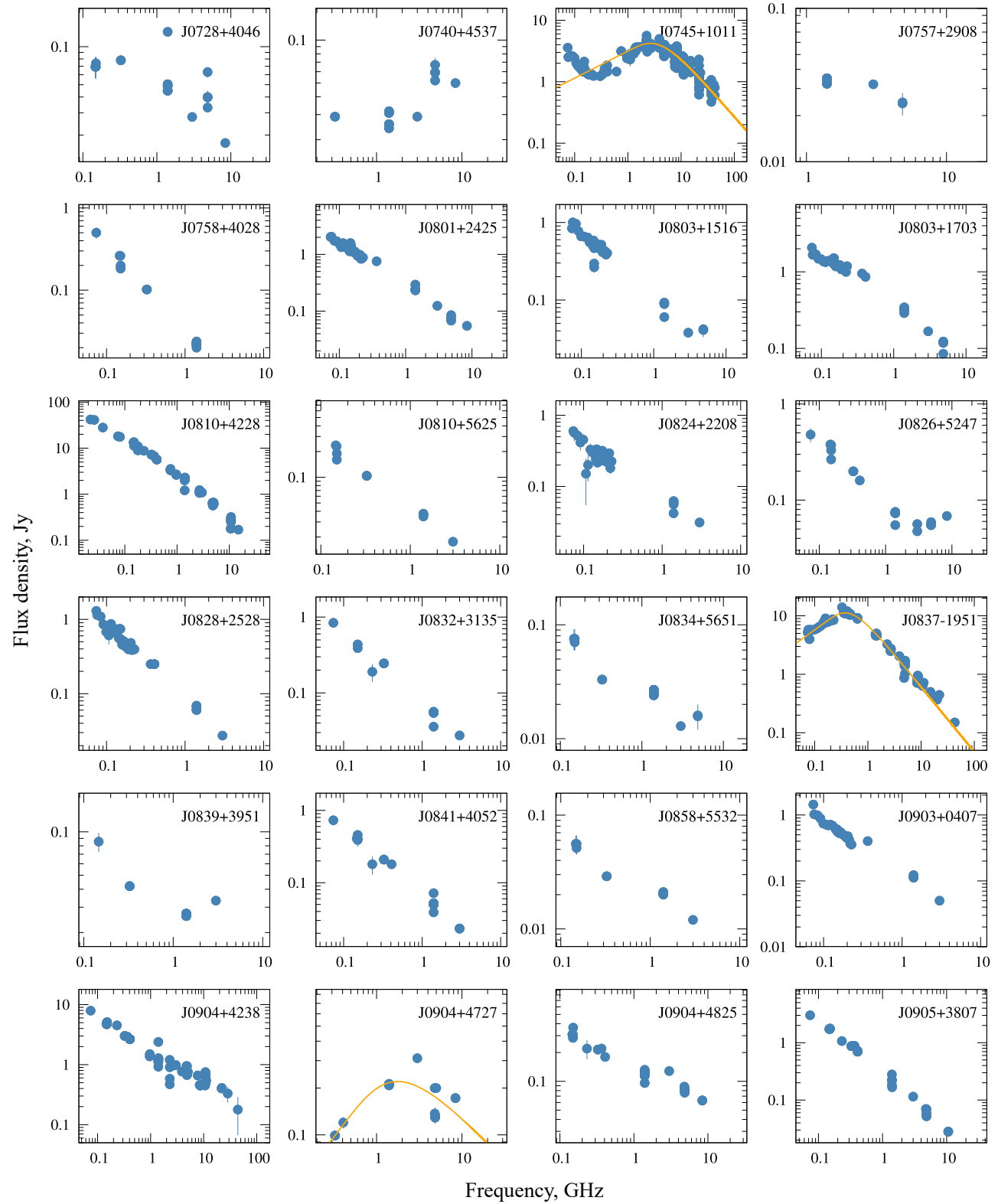
- Afonso J., et al., 2011, *ApJ*, **743**, 122
- Aller M. F., Aller H. D., Hughes P. A., 1992, *ApJ*, **399**, 16
- An T., Wang A., Zhang Y., Aditya J. N. H. S., Hong X., Cui L., 2022, *MNRAS*, **511**, 4572
- Balayan S. K., Verkhodanov O. V., 2004, *Astrophysics*, **47**, 505
- Becker R. H., White R. L., Helfand D. J., 1994, in Crabtree D. R., Hanisch R. J., Barnes J., eds, Astronomical Society of the Pacific Conference Series Vol. 61, Astronomical Data Analysis Software and Systems III. p. 165
- Bryant J. J., Johnston H. M., Broderick J. W., Hunstead R. W., De Breuck C., Gaensler B. M., 2009, *A&ARv*, **395**, 1099
- Bursov N. N., Lipovka N. M., Soboleva N. S., Temirova A. V., Gol’Neva N. E., Parijskaya E. Y., Savastenyuk A. V., 1996, Bulletin of the Special Astrophysics Observatory, **42**, 5
- Callingham J. R., et al., 2017, *ApJ*, **836**, 174
- Cohen A. S., Lane W. M., Cotton W. D., Kassim N. E., Lazio T. J. W., Perley R. A., Condon J. J., Erickson W. C., 2007, *AJ*, **134**, 1245
- Condon J. J., Cotton W. D., Greisen E. W., Yin Q. F., Perley R. A., Taylor G. B., Broderick J. J., 1998, *AJ*, **115**, 1693
- Coppejans R., Cseh D., Williams W. L., van Velzen S., Falcke H., 2015, *MNRAS*, **450**, 1477
- Coppejans R., et al., 2016a, *MNRAS*, **459**, 2455
- Coppejans R., et al., 2016b, *MNRAS*, **463**, 3260
- Coppejans R., et al., 2017, *MNRAS*, **467**, 2039
- D’Abrusco R., et al., 2019, *ApJS*, **242**, 15
- Dallacasa D., Stanghellini C., Centonza M., Fanti R., 2000, *A&A*, **363**, 887
- De Breuck C., van Breugel W., Röttgering H. J. A., Miley G., 2000, *A&AS*, **143**, 303
- De Breuck C., et al., 2010, *ApJ*, **725**, 36
- Douglas J. N., Bash F. N., Bozian F. A., Torrence G. V., Wolfe C., 1996, *AJ*, **111**, 1945
- Edwards P. G., Tingay S. J., 2004, *A&A*, **424**, 91
- Falcke H., Körding E., Nagar N. M., 2004, *New Astron. Rev.*, **48**, 1157
- Fan J. H., et al., 2007, *A&A*, **462**, 547

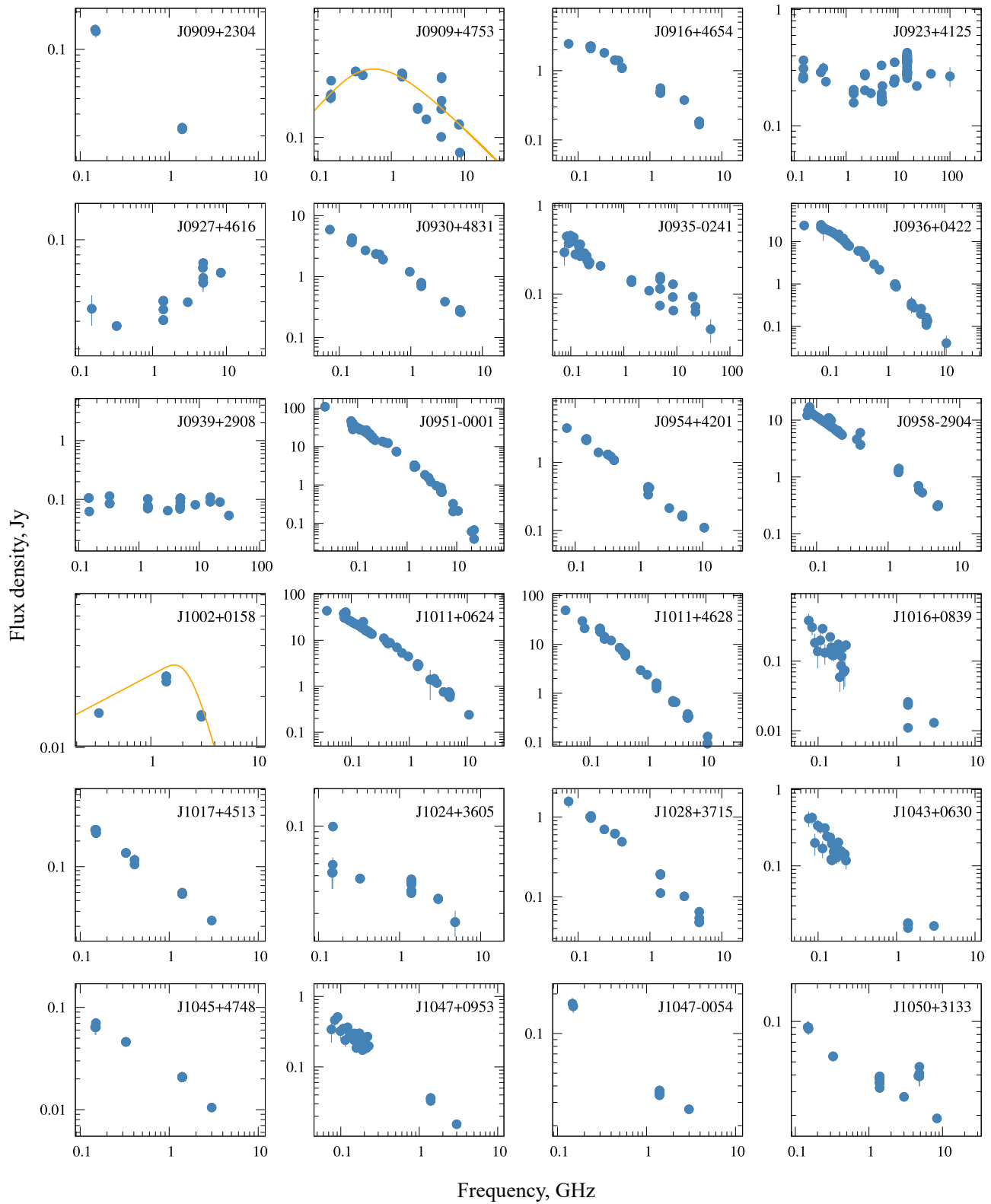
- Fanti R., Fanti C., Schilizzi R. T., Spencer R. E., Nan Rendong Parma P., van Breugel W. J. M., Venturi T., 1990, *A&A*, **231**, 333
- Frey S., Paragi Z., Gurvits L. I., Cseh D., Gabányi K. É., 2010, *A&A*, **524**, A83
- Gabányi K. É., et al., 2021, *Astronomische Nachrichten*, **342**, 1092
- Gendre M. A., Wall J. V., 2008, *MNRAS*, **390**, 819
- Ghisellini G., Celotti A., Tavecchio F., Haardt F., Sbarato T., 2014, *MNRAS*, **438**, 2694
- Ginsburg A., et al., 2019, *AJ*, **157**, 98
- Gorokhov V. L., Verkhodanov O. V., 1994, *Astronomy Letters*, **20**, 671
- Gower J. F. R., Scott P. F., Wills D., 1967, *Mem. RAS*, **71**, 49
- Gregory P. C., Scott W. K., Douglas K., Condon J. J., 1996, *ApJS*, **103**, 427
- Harwood J. J., Hardcastle M. J., Croston J. H., Goodger J. L., 2013, *MNRAS*, **435**, 3353
- Harwood J. J., Hardcastle M. J., Croston J. H., 2015, *MNRAS*, **454**, 3403
- Healey S. E., Romani R. W., Taylor G. B., Sadler E. M., Ricci R., Murphy T., Ulvestad J. S., Winn J. N., 2007, *ApJS*, **171**, 61
- Healey S. E., et al., 2008, *ApJS*, **175**, 97
- Hurley-Walker N., et al., 2017, *MNRAS*, **464**, 1146
- Intema H. T., Jagannathan P., Mooley K. P., Frail D. A., 2017, *A&A*, **598**, A78
- Jarrett T. H., et al., 2011, *AJ*, **735**, 33
- Kellermann K. I., 1964, *ApJ*, **140**, 969
- Kellermann K. I., Pauliny-Toth I. I. K., Williams P. J. S., 1969, *ApJ*, **157**, 1
- Kellermann K. I., Sramek R., Schmidt M., Shaffer D. B., Green R., 1989, *AJ*, **98**, 1195
- Ker L. M., Best P. N., Rigby E. E., Röttgering H. J. A., Gendre M. A., 2012, *MNRAS*, **420**, 2644
- Khabibullina M. L., Verkhodanov O. V., 2009a, *Astrophysical Bulletin*, **64**, 123
- Khabibullina M. L., Verkhodanov O. V., 2009b, *Astrophysical Bulletin*, **64**, 276
- Khabibullina M. L., Verkhodanov O. V., 2009c, *Astrophysical Bulletin*, **64**, 340
- Khabibullina M. L., Verkhodanov O. V., Parijskij Y. N., 2008, *Astrophysical Bulletin*, **63**, 95
- Kiikov S. O., Mingaliev M. G., Stolyarov V. A., Stupalov M. S., 2002, *Bulletin of the Special Astrophysics Observatory*, **54**, 5
- Klamer I. J., Ekers R. D., Bryant J. J., Hunstead R. W., Sadler E. M., De Breuck C., 2006, *MNRAS*, **371**, 852
- Kopylov A. I., Goss W. M., Parijskij Y. N., Soboleva N. S., Verkhodanov O. V., Temirova A. V., Zhelenkova O. P., 2006, *Astronomy Letters*, **32**, 433
- Kovalev Y. Y., Nizhelsky N. A., Kovalev Y. A., Berlin A. B., Zhekanis G. V., Mingaliev M. G., Bogdantsov A. V., 1999, *A&AS*, **139**, 545
- Kraus A., et al., 2003, *A&A*, **401**, 161
- Krogager J. K., et al., 2018, *ApJS*, **235**, 10
- Labiano A., Barthel P. D., O'Dea C. P., de Vries W. H., Pérez I., Baum S. A., 2007, *A&A*, **463**, 97
- Lacy M., et al., 2004, *ApJS*, **154**, 166
- Lacy M., et al., 2020, *PASP*, **132**, 035001
- Lazio T. J. W., Waltman E. B., Ghigo F. D., Fiedler R. L., Foster R. S., Johnston K. J., 2001, *ApJS*, **136**, 265
- Liu Y., Jiang D. R., Gu M., Gurvits L. I., 2016, *Astronomische Nachrichten*, **337**, 101
- Lyke B. W., et al., 2020, *ApJS*, **250**, 24
- Majorova E. K., 2008, *Astrophysical Bulletin*, **63**, 56
- Marscher A. P., et al., 2008, *Nature*, **452**, 966
- Matthews T. A., Morgan W. W., Schmidt M., 1964, *ApJ*, **140**, 35
- Mauch T., Klöckner H.-R., Rawlings S., Jarvis M., Hardcastle M. J., Obreschkow D., Saikia D. J., Thompson M. A., 2013, *MNRAS*, **435**, 650
- Miley G., De Breuck C., 2008, *A&ARv*, **15**, 67
- Mingaliev M. G., Botashev A. M., Stolyarov V. A., 1998, *Bulletin of the Special Astrophysics Observatory*, **46**, 28
- Mingaliev M. G., Stolyarov V. A., Davies R. D., Melhuish S. J., Bursov N. A., Zhekanis G. V., 2001, *A&A*, **370**, 78
- Mingaliev M. G., Sotnikova Y. V., Torniainen I., Tornikoski M., Uдовитский R. Y., 2012, *A&A*, **544**, A25
- Mingaliev M. G., Sotnikova Y. V., Mufakharov T. V., Erkenov A. K., Uдовитский R. Y., 2013, *Astrophysical Bulletin*, **68**, 262
- Mingaliev M., et al., 2017, *Astronomische Nachrichten*, **338**, 700
- Morabito L. K., Harwood J. J., 2018, *MNRAS*, **480**, 2726
- Mufakharov T., Mikhailov A., Sotnikova Y., Mingaliev M., Stolyarov V., Erkenov A., Nizhelskij N., Tsybulev P., 2021, *MNRAS*, **503**, 4662
- Murphy T., et al., 2010, *MNRAS*, **402**, 2403
- Nesvadba N. P. H., De Breuck C., Lehnert M. D., Best P. N., Collet C., 2017, *A&A*, **599**, 44
- O'Dea C. P., 1990, *MNRAS*, **245**, 20P
- O'Dea C. P., 1998, *PASP*, **110**, 493
- O'Dea C. P., Baum S. A., 1997, *AJ*, **113**, 148
- O'Dea C. P., Saikia D. J., 2021, *A&ARv*, **29**, 3
- O'Dea C. P., Baum S. A., Morris G. B., 1990, *A&AS*, **82**, 261
- O'Dea C. P., Baum S. A., Stanghellini C., 1991, *ApJ*, **380**, 66
- Ochsenbein F., Bauer P., Marcout J., 2000, *A&AS*, **143**, 23
- Pacholczyk A. G., 1970, *Radio astrophysics. Nonthermal processes in galactic and extragalactic sources*
- Parijskij Y. N., Goss W. M., Verkhodanov O. V., Kopylov A. I., Soboleva N. S., Temirova A. V., 1999, *Astrophysical Bulletin*, **48**, 5
- Parijskij Y. N., et al., 2014, *MNRAS*, **439**, 2314
- Páris I., et al., 2018, *A&A*, **613**, 17
- Planck Collaboration 2016, *A&A*, **594**, A13
- Planck Collaboration et al., 2011, *A&A*, **536**, A14
- Ramasawmy J., et al., 2021, *A&A*, **648**, A14
- Randall K. E., Hopkins A. M., Norris R. P., Edwards P. G., 2011, *MNRAS*, **416**, 1135
- Rengelink R. B., Tang Y., de Bruyn A. G., Miley G. K., Bremer M. N., Roettgering H. J. A., Bremer M. A. R., 1997, *A&AS*, **124**, 259
- Richards J. L., et al., 2011, *ApJS*, **194**, 29
- Romani R. W., Sowards-Emmerd D., Greenhill L., Michelson P., 2004, *ApJ*, **610**, L9
- Sadler E. M., et al., 2006, *MNRAS*, **371**, 898
- Sadler E. M., Chhetri R., Morgan J., Mahony E. K., Jarrett T. H., Tingay S., 2019, *MNRAS*, **483**, 1354
- Sanghera H. S., Saikia D. J., Luedke E., Spencer R. E., Foulsham P. A., Akujor C. E., Tzioumis A. K., 1995, *A&A*, **295**, 629
- Sbarato T., Ghisellini G., Tagliaferri G., Foschini L., Nardini M., Tavecchio F., Gehrels N., 2015, *MNRAS*, **446**, 2483
- Seymour N., et al., 2007, *ApJS*, **171**, 353
- Singh V., et al., 2014, *A&A*, **569**, A52
- Smolčić V., et al., 2014, *MNRAS*, **443**, 2590
- Snellen I. A. G., Schilizzi R. T., de Bruyn A. G., Miley G. K., Rengelink R. B., Roettgering H. J., Bremer M. N., 1998, *A&AS*, **131**, 435
- Snellen I. A. G., Lehnert M. D., Bremer M. N., Schilizzi R. T., 2002, *MNRAS*, **337**, 981
- Solovyov D. I., Verkhodanov O. V., 2014a, *Astronomy Letters*, **40**, 606
- Solovyov D. I., Verkhodanov O. V., 2014b, *Astronomy Reports*, **58**, 506
- Sotnikova Y. V., Mufakharov T. V., Majorova E. K., Mingaliev M. G., Uдовитский R. Y., Bursov N. N., Semenova T. A., 2019, *Astrophysical Bulletin*, **74**, 348
- Sotnikova Y., et al., 2021, *MNRAS*, **508**, 2798
- Souchay J., et al., 2015, *A&A*, **583**, 9
- Spingola C., Dallacasa D., Belladitta S., Caccianiga A., Giroletti M., Moretti A., Orienti M., 2020, *A&A*, **643**, L12

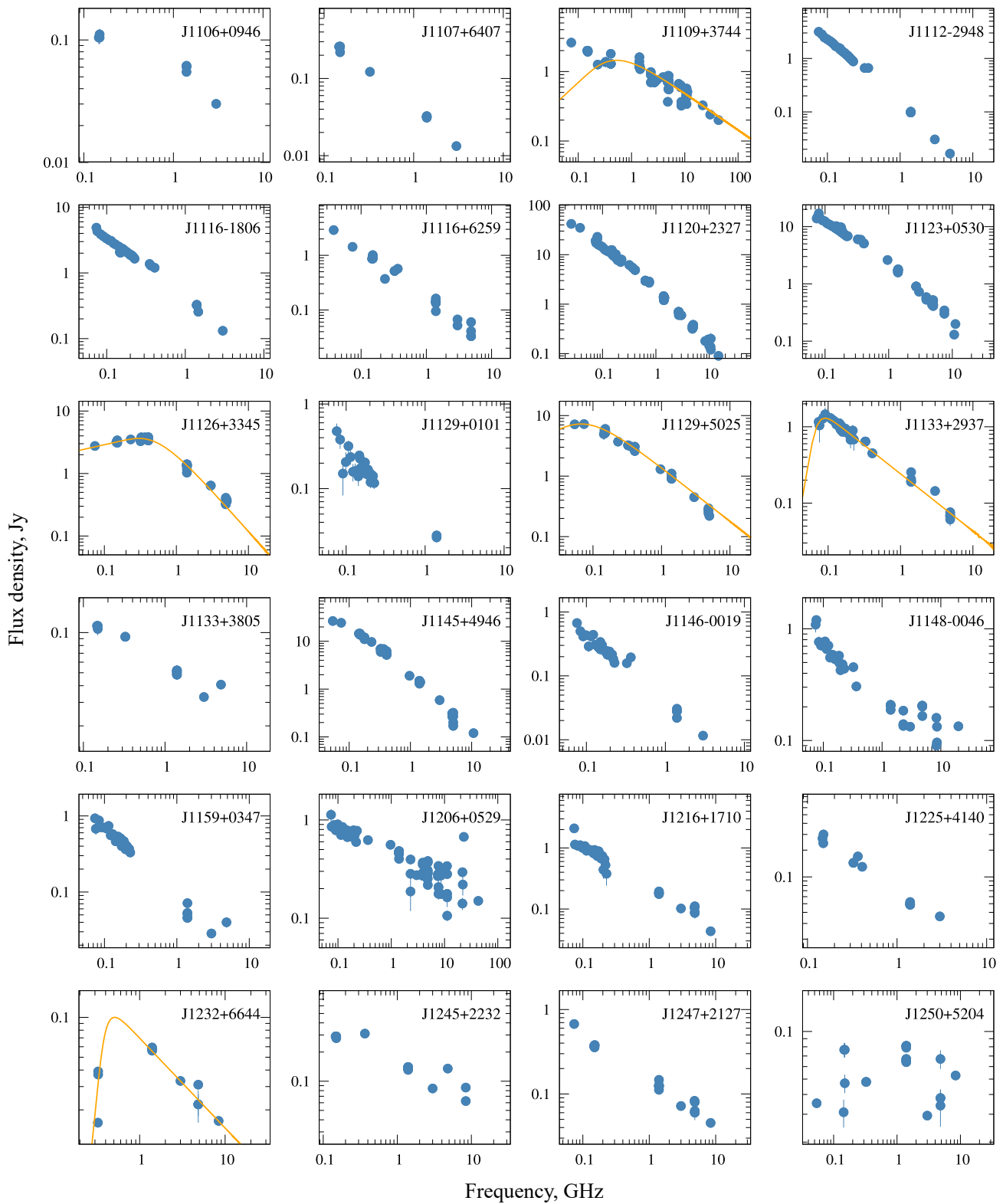
- Spoelstra T. A. T., Patnaik A. R., Gopal-Krishna 1985, *A&A*, **152**, 38
- Stern D., Dey A., Spinrad H., Maxfield L., Dickinson M., Schlegel D., González R. A., 1999, *AJ*, **171**, 1122
- Stern D., et al., 2005, *ApJ*, **631**, 163
- Stern D., et al., 2012, *ApJ*, **753**, 18
- Tielens A. G. G. M., Miley G. K., Willis A. G., 1979, *A&AS*, **35**, 153
- Tornikoski M., Lainela M., Valtaoja E., 2000, *AJ*, **120**, 2278
- Trushkin S. A., 2003, *Astrophysical Bulletin*, **55**, 90
- Tucci M., et al., 2008, *MNRAS*, **386**, 1729
- Türler M., Courvoisier T. J. L., Paltani S., 1999, *A&A*, **349**, 45
- Verkhodanov O. V., 1994, *Astronomy Reports*, **38**, 307
- Verkhodanov O. V., 1997, in "Problems of Modern Radio Astronomy". p. 322
- Verkhodanov O. V., Parijskij Y., 2008, *Fiz.Mat.Lit.*
- Verkhodanov O. V., Trushkin S. A., 2000, *Astrophysical Bulletin*, **50**, 115
- Verkhodanov O. V., Verkhodanova N. V., 1999, *Astronomy Reports*, **43**, 417
- Verkhodanov O. V., Trushkin S. A., Chernyakov V. N., 1997, *Baltic Astronomy*, **6**, 275
- Verkhodanov O. V., Kopylov A. I., Parijskij Y. N., Soboleva N. S., Temirova A. V., 1999, *Astrophysical Bulletin*, **48**, 41
- Verkhodanov O. V., Opylov A. I., Zhelenkova O. P., Verkhodanova N. V., Chernyakov V. N., Parijskij Y., Soboleva N. S., Temirova A. V., 2000a, *Atsron. Astrophys. Trans.*, **19**, 663
- Verkhodanov O. V., Andernach H., Verkhodanova N. V., 2000b, *Astrophysical Bulletin*, **29**, 53
- Verkhodanov O. V., Parijskij Y. N., Soboleva N. S., Kopylov A. I., Temirova A. V., Zhelenkova O. P., Goss W. V., 2001, *Astrophysical Bulletin*, **52**, 3
- Verkhodanov O. V., Chavushyan V. H., Mújica R., Trushkin S. A., Valdés J. R., 2003, *Astronomy Reports*, **47**, 119
- Verkhodanov O. V., Trushkin S. A., Andernach H., Chernyakov V. N., 2005, *Bulletin of the Special Astrophysics Observatory*, **58**, 118
- Verkhodanov O. V., Khabibullina M. L., Singh M., Pirya A., Verkhodanova N. V., Nandi S., 2008, in *Problems of Practical Cosmology*, Volume 2. pp 247–450
- Verkhodanov O. V., Verkhodanova N. V., Andernach H., 2009, *Astrophysical Bulletin*, **64**, 72
- Verkhodanov O. V., Kozlova D. D., Sotnikova Y. V., 2018, *Astrophysical Bulletin*, **73**, 393
- White G. J., et al., 2012, *MNRAS*, **427**, 1830
- Wright A. E., Wark R. M., Troup E., Otrupcek R., Jennings D., Hunt A., Cooke D. J., 1991, *MNRAS*, **251**, 330
- Wright E. L., et al., 2010, *AJ*, **140**, 1868
- Wrobel J. M., Patnaik A. R., Browne I. W. A., Wilkinson P. N., 1998, in *American Astronomical Society Meeting Abstracts*. p. 40.04
- de Vries W. H., Barthel P. D., O'Dea C. P., 1997, *A&A*, **321**, 105
- van Breugel W., De Breuck C., Stanford S. A., Stern D., Röttgering H., Miley G., 1999, *ApJ*, **518**, L61

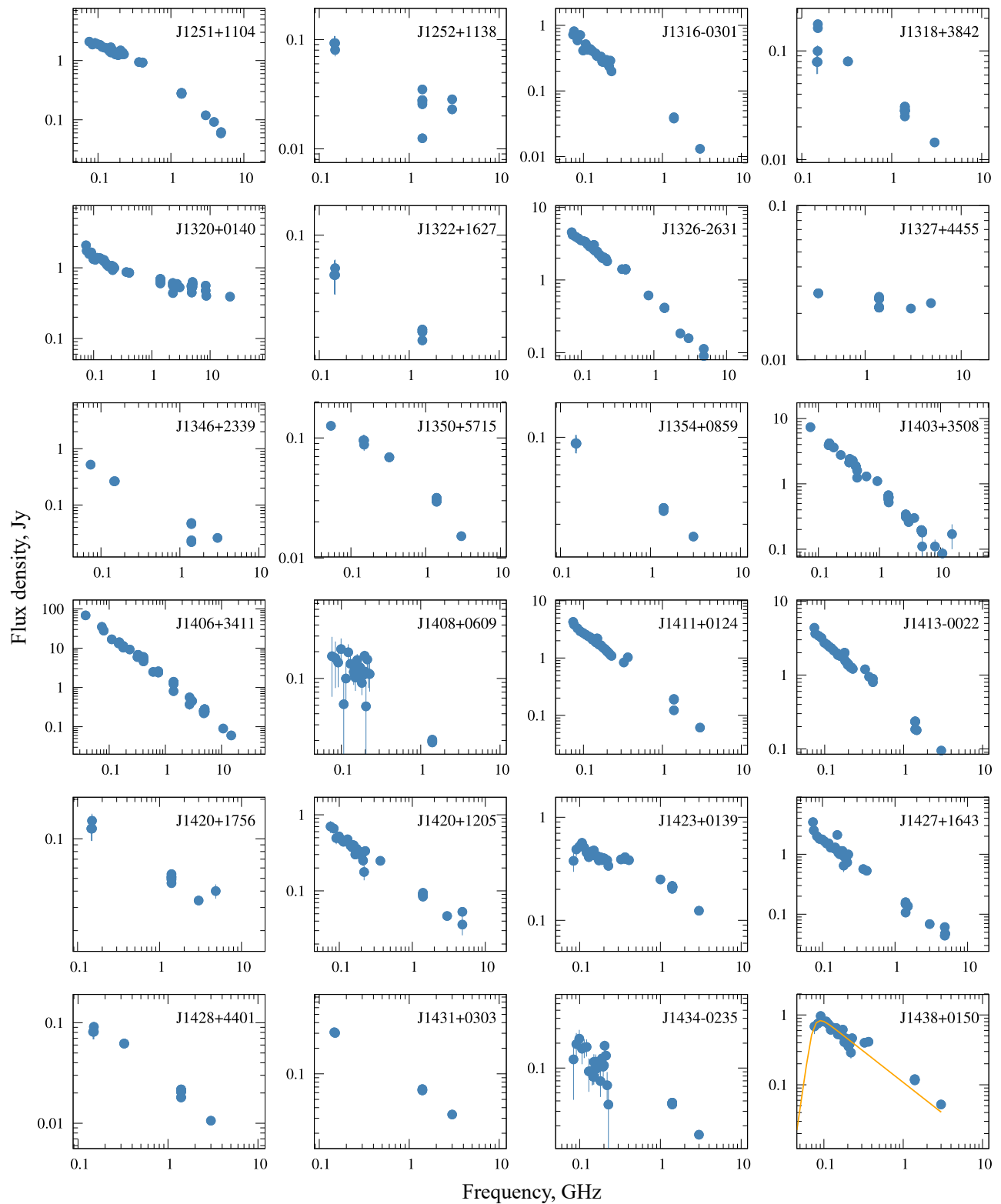
APPENDIX A: THE RADIO CONTINUUM SPECTRA OF THE GALAXIES.

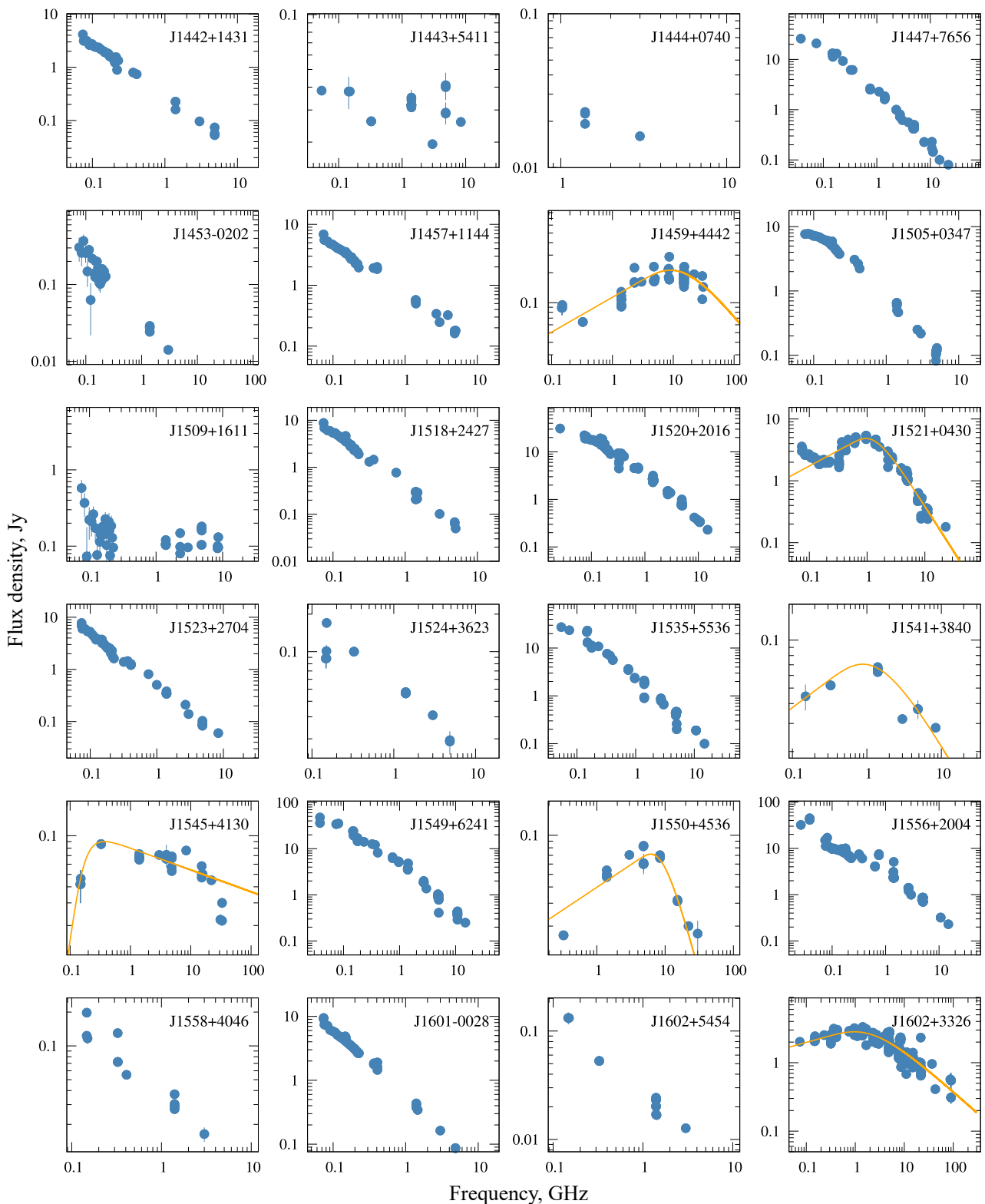
**Figure A1.** The radio continuum spectra of the galaxies.

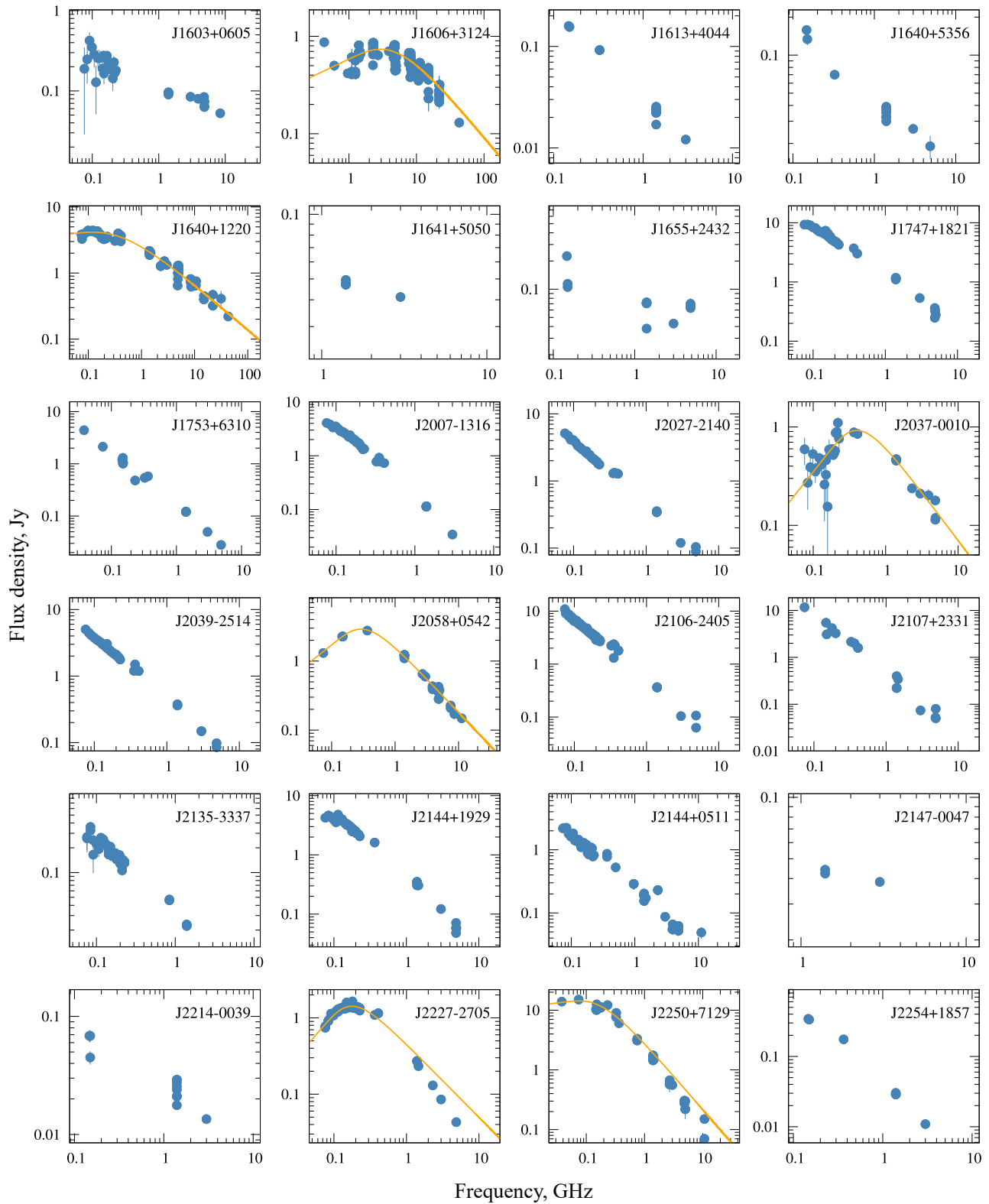
**Figure A1.** (Contd.)

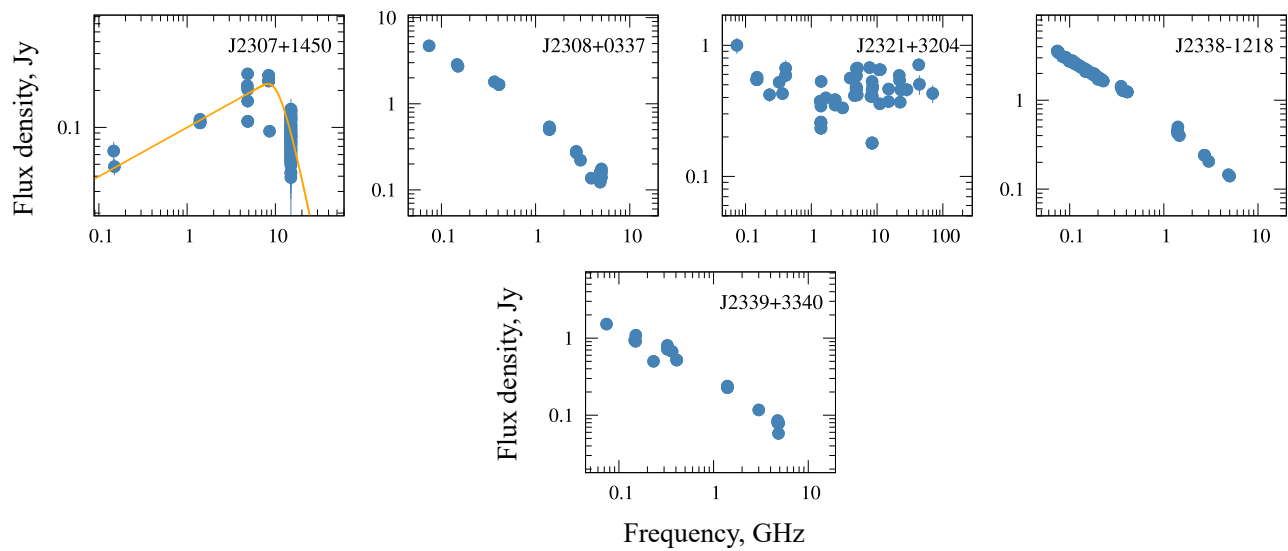
**Figure A1.** (Contd.)

**Figure A1.** (Contd.)

**Figure A1.** (Contd.)

**Figure A1.** (Contd.)

**Figure A1.** (Contd.)

**Figure A1.** (Contd.)

